InAs/AlSb Based Mid-Infrared QCL Growth and XRD Simulation

by

Xueren Wang

A thesis
presented to the University of Waterloo
in fulfillment of the
thesis requirement for the degree of
Master of Applied Science
in
Electrical and Computer Engineering

Waterloo, Ontario, Canada, 2016

I hereby declare that I am the sole author of this thesis. This is a true copy of the thesis, including any required final revisions, as accepted by my examiners.

I understand that my thesis may be made electronically available to the public.

Abstract

In the past two decades, mid-infrared (MIR) quantum cascade laser (QCL) research has been rapidly developed and has resulted in an enabling platform for the remote sensing and metrology. QCL is designed by spatial confinement in quantum well structures on a nanometer scale, enabling the transitions between the electron confined states. In order to obtain the particular characteristics via quantum engineering, the material growth needs to be precisely controlled across the large number of layers. In this work, the growth condition of InAs/AlSb based MIR-QCL, grown by molecular beam epitaxy (MBE), is investigated. A low defect density growth result is observed by employing the optimized growth condition. Laser devices with disk mesa or ridge waveguide are fabricated, and the further electrical characterization exhibits the device lasing at 3.4 μm with a threshold current density of around 2.1 kA/cm^2. The superlattice average layer thickness is determined by using high resolution X-ray diffraction (HRXRD), which is considered as one of the non-destructive analysis technique to extract the information about the thin film constructions. Comprehensive modeling built and simulation results are analyzed and discussed based on the HRXRD ω-2θ scanning curve, yielding valuable information about the full structure device growth result. The interface related simulations are performed by using RADS software to investigate the relationship between the strain distribution and the relative intensities of the SL reflections in XRD.

Acknowledgements

I would like to express my deepest gratitude to all the people who made this work possible.

My deepest thanks go to my supervisors Dr. Dayan Ban and Dr. Zbigniew Wasilewski, for providing guidance and encouragement, and their help in troubleshooting this thesis.

I would like to extend my thanks to Dr. Denise Gosselink. She is meticulous in her approach and has an unparalleled talent for synthesizing research results. I learned a great deal from her careful attention to details, and analytical rigor.

Thanks to all my colleges in the past and present for the contribution to the research that underpins this work. I would like to thank Chao Xu for the FTIR characterization guidance, Dr. Dennis Striakhilev and Siyi Wang for the cleaning room device fabrication support, Xiaoliang He for the unremitting efforts made to the device LIV measurement, Dr. Seyed Ghasem Razavipour, Boyu Wen, Yue Zhuo, Julie Tournet, Yinqiu Shi, Alan Tam and Christopher Deimert for the fruitful discussions and valuable comments.

The last, but certainly not least, I would like thank my family for the boundless support in my life. My deepest gratitude and love to my parents and my sister!

Table of Contents

List of Figures

List of Tables

List of Acronyms

BEP	Beam equivalent pressure
BET	Band-edge thermometry
DIC	Differential interference contrast
FET	Field effect transistor
FTIR	Fourier transform infrared spectrometer
GOF	Good of fitness
HAADF	High-angle annular dark field
HEMT	High-electron-mobility transistors
HRXRD	High resolution X-ray diffraction
ICL	Interband cascade laser
LIV	Light current voltage
MBE	Molecular beam epitaxy
MIR	Mid-infrared
PECVD	Plasma enhanced vapor deposition
PL	Photoluminescence
PVCR	Peak-to-valley current ratio
QCL	Quantum cascade laser
RADS	Rocking-Curve Analysis by Dynamical Simulation (software)
RGA	Residual gas analyser
RHEED	Reflection high-energy electron diffraction
SEM	Scanning electron microscopy

SIMS	Secondary ion mass spectroscopy
SL	Superlattice
TEM	Transmission electron microscopy
UHV	Ultra high vacuum
XPS	X-ray photoelectron spectroscopy
XRD	X-ray Diffraction
XSTM	Cross-sectional scanning tunneling microscopy

Chapter 1

Introduction

Quantum cascade laser (QCL) was demonstrated for the first time in 1994 by J. Faist *et al* [1]. Since then, it has been rapidly developed from the limited cryogenic lasing temperature at the very beginning, to the room temperature operation [2], from the limited low-duty-cycle pulsed operation to the continuous-wave operation [3]. Applying the advanced quantum engineering, the QCL which can simultaneously emit at multiple wavelengths or is capable of broadband tuning have been recently demonstrated as well [4-5]. Although these versatile QCLs have already been fabricated successfully, the research, such as utilizing different material system and engineering differently the lasing levels, is never stopped to further improve the device performance. In this project, the growth condition optimization is mainly focused to achieve smooth surface and low interface roughness.

Since the laser materials and interface control are highly relevant to the device performance, lattice matched material systems are preferred for the QCL growth. Figure 1.1 shows part of the suitable material choices for the QCL design with the lasing wavelength less than 5 μm [6]. Lattice matched $Ga_{0.47}In_{0.53}As/Al_{0.48}In_{0.52}As$ structure grown on InP substrate was the material selection for the first QCL device [1] (I in figure 1.1) lasing at 4.2 μm. Followed by the same

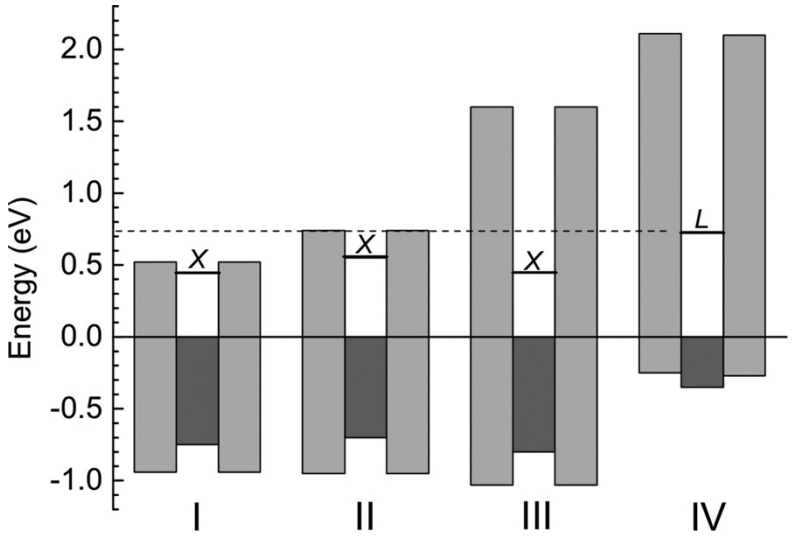

Figure 1.1 Band offsets in (I) $Ga_{0.47}In_{0.53}As/Al_{0.48}In_{0.52}As/InP$, (II) $Ga_{0.3}In_{0.7}As/Al_{0.6}In_{0.4}As/InP$, (III) $Ga_{0.47}In_{0.53}As/AlSb_{0.44}As_{0.56}As/InP$, and (IV) InAs/AlSb/InAs material systems, which are suitable for the QCL emission wavelength less than 5 μm fabrication. X and L represent the energy position of lateral minima in the conduction band of the well material [6].

$Ga_xIn_{1-x}As/Al_yIn_{1-y}As$ material system, strain-compensated concept was first introduced into the QCL design which enabled a larger conduction band discontinuity by decreasing the Ga content to 0.3 and increasing the Al concentration to 0.6, as shown in figure1.1 II [7]. The compressive strain provided by the larger lattice constant layer can be compensated by the equal magnitude tensile strain, introduced by smaller lattice constant layer. As long as each layer is grown under its critical layer thickness (which would be discussed in latter section), by growing alternating layers of opposite strain, thick stacks can be growth with a balanced stress between each two layers. By replacing the barrier material with AlSbAs, QCL emission wavelength as short as 3.05 μm was demonstrated (III in figure 1.1) [8]. IV in figure 1.1 shows the band offsets in InAs/AlSb material system. The conduction band discontinuity between those two materials is approximately 2.1 eV, which enables large energies of intersubband transitions contributing to the short wavelength QCL design [9]. Another reason to choose InAs/AlSb material system is based on its large direct-indirect valley separation in InAs, which is larger than any of the structures shown in figure 1.1 grown on InP. If the Γ-minimum of the

conduction band are close to the lateral valleys, X or L, electrons from the upper lasing state can be scattered into the indirect valley and thus disrupt operation of the device, which affects the QCL performance. Hence, both of the larger conduction band offset and Γ-X or L separation are desired for the short wavelength QCL operation [10].

The growth of InAs/AlSb material system requires the simultaneous change of group III and group V elements across the interface, which introduces its own set of challenges. However, due to the similar lattice constant ~1.3 % misfit between InAs and AlSb, and the advantages of this material system for short wavelength QCL operation, InAs/AlSb material system is highly attractively. Since there are no common atoms between the barrier and well, the interfaces consist of either Al-As bonds or In-Sb bonds. Interfaces can thus be Al-As type, In-Sb type, or mixed type. The misfit between InAs (the substrate) and AlAs or InSb is -6.6% or +6.9%, respectively. The interfaces themselves can therefore be considerably strained, which can affect the device properties through an increasing of interface roughness or a modification of the band structure [11]. Hence, the study of interface structure within InAs/AlSb material system is highly desirable not only from the material science point of view, but also for the optimization of QCL devices performance.

In order to characterize the interface properties of InAs/AlSb structures, numerous probing techniques were employed, such as photoluminescence (PL) [12-13], ellipsometry [14], Hall effect measurement [15-16], Raman scattering [17-18], X-ray diffraction (XRD) [19], cross-sectional scanning tunneling microscopy (XSTM) [20] and transmission electron microscopy (TEM) [11] [21]. In this project, high resolution X-ray diffraction (HRXRD) is mainly used. We introduced a simple model based on Jordan Valley RADS software to simulate high resolution XRD diagram of the full InAs/AlSb MIR-QCL structure.

There are two focal points for this thesis. One is the study of InAs/AlSb based MIR-QCL growth by MBE, and the other is the investigation of interface structure with InAs/AlSb heterostructures by means of HRXRD experiments and simulation. In Chapter 2, a brief overview of MIR-QCL, crystal lattice theory and SL related X-ray diffraction calculation are presented. In Chapter 3, the main features of MBE technique as well as in-situ, ex-situ

characterization tools, experimental procedures as well as device fabrication and testing used in this work are introduced. In Chapter 4, both of the growth related result and the study by XRD simulation are explained in details. The main findings and potential future research directions are discussed in Chapter 5.

Chapter 2

Background Theory

In this chapter the theoretical background of this thesis is presented. In section 2.1, the basic theory of mid-infrared quantum cascade laser is presented. Basic crystallography is presented in section 2.2, and finally the basic theory of X-ray diffraction is presented in section 2.3.

2.1 Mid-infrared Quantum Cascade Laser

For conventional semiconductor lasers, the optical emission is generated when the high energy electrons in the conduction band recombines with holes in the valence band, called interband transition. The emission wavelength is primarily determined by the bandgap of the semiconductor material, as shown in Figure 2.1(a). However, the lasers based on this transition mechanism can hardly be designed for the mid and far infrared sources because of a small band gap, typically less than 0.1 eV, is required for the corresponding long wavelength emission (10-300 μm).

For further minimizing the “band gap”, Esaki and Tsu introduced the concept of miniband and minigap to describe the electronic state created by a certain repeated sequence of

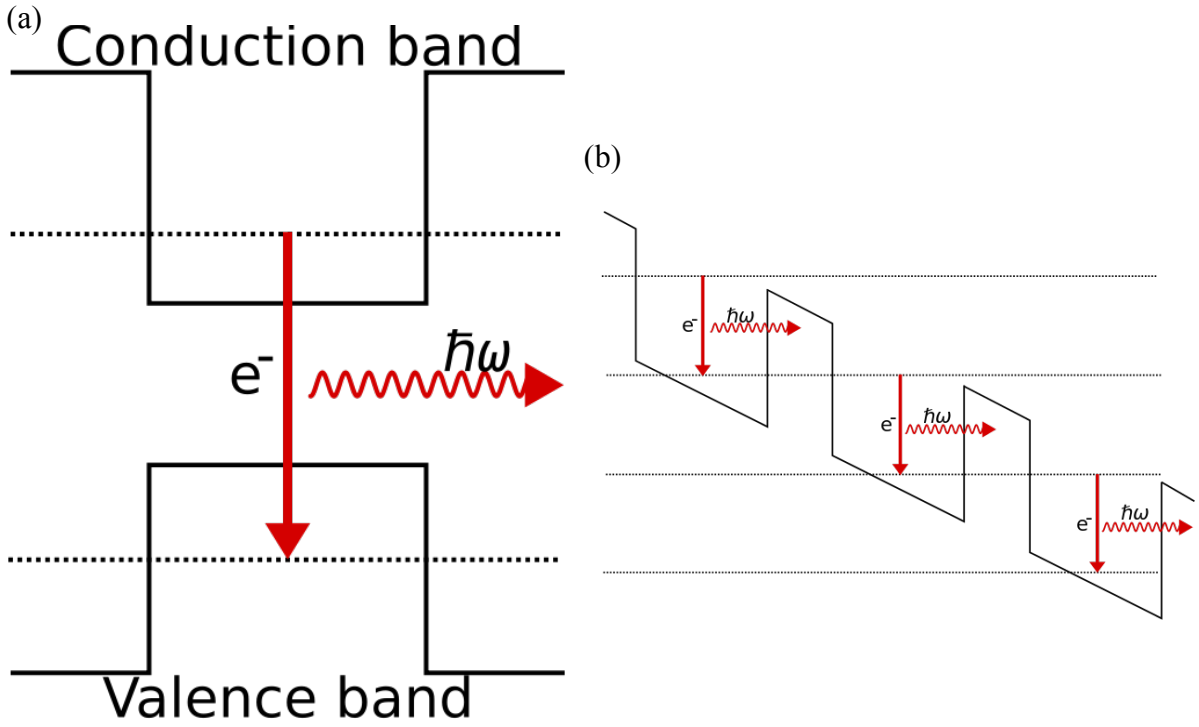

Figure 2.1: (a) Schematic diagram of energy band profile for conventional semiconductor lasers, based on interband transition. (b) Conduction band profile of intersubband transition. It occurs between states that belong to the same band [22-23].

semiconductor layers. The transitions between those confined states are referred to as intersubband transitions, as shown in Figure 2.1 (b). The transition energy is determined by the difference between the energy levels of individual electronic states, and it approaches to zero as the well thickness increases to infinity enabling the design of long-wavelength laser devices. The first laser based on the intersubband transition, called quantum cascade laser (QCL), was demonstrated by Jerome Faist *et al* in Bell Labs in 1994 [1]. I The first QCL device could be operated only at cryogenic temperature and pulsed mode. With the development of the intersubbabnd alignment design and the MBE technique, the first distributed-feedback QCL, which could lase at room temperature, was demonstrated in 1997, while it was lasing in pulsed operation [2]. In 2002, Mattias *et al* reported that they realized the first room temperature mid-infrared QCL lased in continuous wave operation [3], which introduced the

potential applications of QCL in high-resolution spectroscopy, chemical sensing and free-space optical communication systems.

As shown in Figure 2.2, the lasing spectrum of most of the intersubband transition based lasers are located in the mid-infrared range. There are two main reasons. Firstly, near-infrared or visible emissions correspond to a large band gap, which means a large conduction band discontinuity is required for the constituent materials. However, the growth and fabrication of this kind of materials, such as the InGaN/AlN heterostructures, is not mature enough for the high quality and reliable device requirement. Secondly, devices based on the interband transitions are not comparable with the cascade lasers in mid-infrared range in terms of the

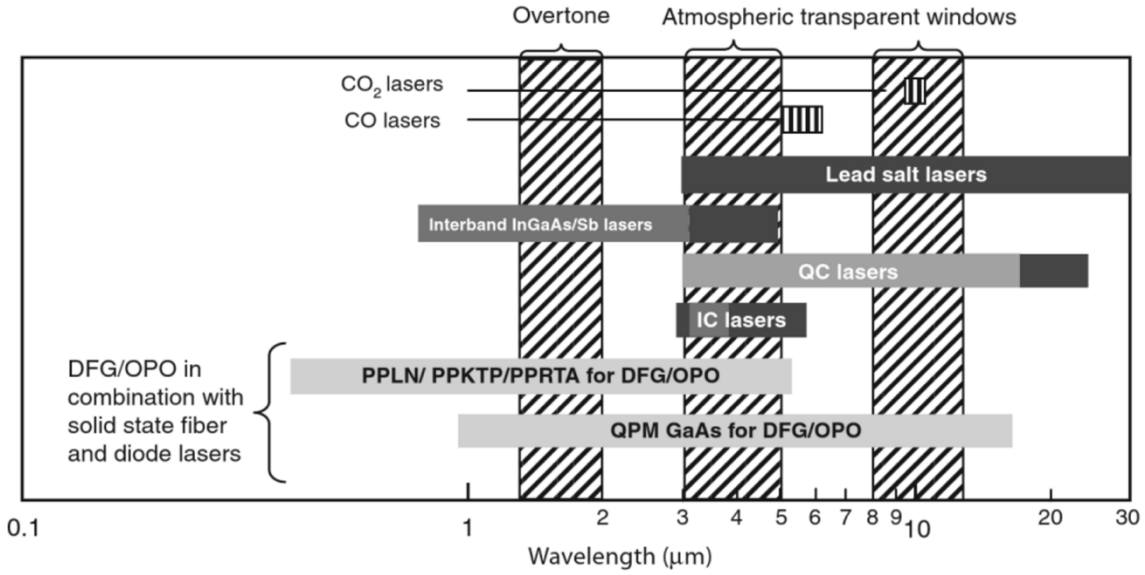

Figure 2.2: Various laser sources and the typical wavelength coverage of these sources. Two atmospheric infrared windows, 3-5 μm and 8-14 μm, are shown as the right two shadow regions, which are typically employed for trace gas sensing. The nonlinear optical parametric frequency conversion based fiber laser sources have been achieved in a large coverage over this spectrum, as the two lower bars shown. CO and CO_2 gas laser sources, generally limited to a certain emission line, are generally used for trace gas detection. The dark and light bars represent the different operating temperature achieved by the semiconductor lasers, which are cryogenic temperature and room temperature, respectively [24].

high temperature and high power applications, which in turn, further stimulates the development of intersubband transition based devices in such a wavelength range.

The lead salt diode lasers are typically comprised of ternary or even quaternary lead compounds. The emission wavelength is directly determined by the material bandgap energy. Before the development of quantum cascade lasers, most of the mid-infrared spectrum were generated by this kind of lasers, as a result of the wide frequency range coverage. However, the low power and requirement of cryogenic operation properties always limit their further application. Interband cascade lasers are similar to QCLs, which also follow the concept of bandstructure engineering to achieve an optimized laser design, while the radiation is based on the interband transition. It was firstly demonstrated by Yang in 1995 [25], and the wavelength had been developed to the range of 2.9 μm to 5.2 μm [26]. Compared with those sources, quantum cascade lasers exhibit the highly superiority in wide wavelength coverage (3-16 μm), room temperature operation and large peak powers.

2.2 Crystal lattices

Crystal is a solid material with the constituents, typically as the atoms and ions, arranged in a highly ordered microscopic structure. It exhibits a perfectly regular three-dimensional arrangement of atoms making up the solid over thousands of atomic radii. A quantitative model is built by considering the crystal is assembled by an infinite three-dimensional repetition of identical 'building block' consisting of a definite arrangement of atoms and each block having an identical orientation, which is also known as the lattice. To simplify this concept, a hypothetical two-dimensional lattice is introduced as shown in Figure 2.3 (a). The start point can be randomly chosen, typically an atomic site, then find two shortest, non-collinear vectors **a** and **b** which origin point to one that is exactly equivalent. Those two vectors are defined as the primitive translation vectors. The primitive unite cell is known as the spaced bounded by considering the parallelogram of **a** and **b** as two sides. Hence the lattice of the crystal can be

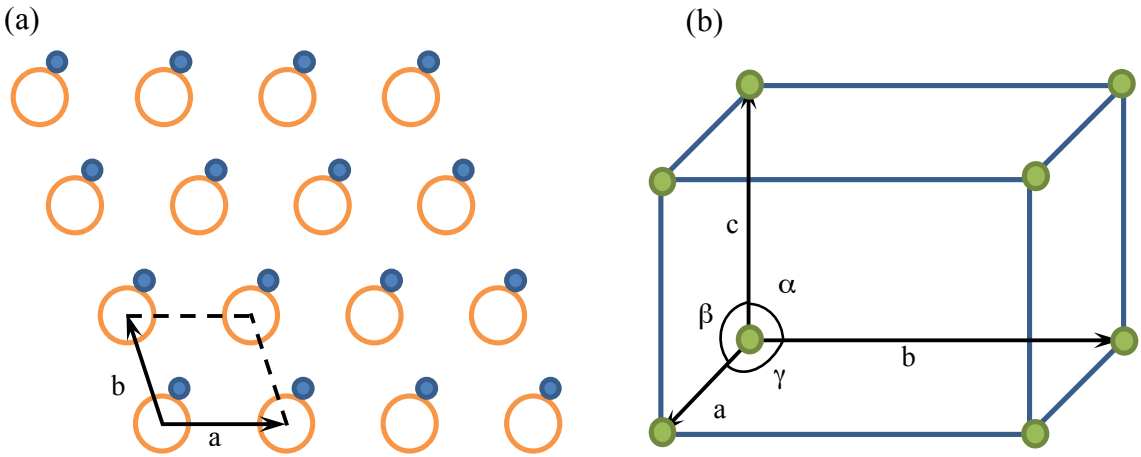

Figure 2.3: (a) Two dimensional unit cell with basis vectors **a** and **b**. (b) Three dimensional unit cell with basis vectors, and angles α, β, γ between each two out of three vectors **a**, **b** and **c**.

constructed by $T = l\boldsymbol{a} + m\boldsymbol{b}$, where l and m are integral values. Specifically, the smallest crystal unit forming the entire periodic structure is defined as the unit cell.

In three-dimensions cases as shown in Figure 2.3 (b), where the centers of these atoms or the clusters of atoms are simplified as the lattice points, T will have the form

$$T = l\boldsymbol{a} + m\boldsymbol{b} + n\boldsymbol{c} \tag{2.1}$$

where **a**, **b**, **c** are there non-collinear, co-planar vectors, and l, m, n are integral values.

2.2.1 Crystal planes

For further identification of a crystal, some special notation is generally used, such as the positions of atoms within the unit cell, planes directions within the crystal and the orientations of the various planes of atoms.

Within the unit cell, the position r of an atom is determined refer to the corner of the cell. Assuming the unit vectors of the cell are **a**, **b** and **c**, then we have

$$r = u\boldsymbol{a} + v\boldsymbol{b} + w\boldsymbol{c} \tag{2.2}$$

where u, v, w are numbers which are equal or smaller than 1. Then the coordinate of this atom is said to be (u, v, w).

In terms of the plain identification, Miller indices concept is introduced. Firstly, find the intercepts of the plane on the crystal axes. Take reciprocals of these three numbers, then reduce those three values to the smallest three integers by multiplying each by the smallest common denominator. The final three number h, k, l represents as the Miller indices (hkl) of the plane and all other planes which are parallel to it and space by the distance d expressed as in Eq.2.3. Hence all crystal planes related problems can be reduced to the discussion based on a single unit cell with certain plains passing through it.

In general, we use curly brackets $\{hkl\}$ enclose the Miller indices to indicate all planes that are equivalent in the crystal. For example, the planes $\{100\}$ in the cube signify the set of all cube faces (100), (010), (001), $(\bar{1}00)$, $(0\bar{1}0)$ and $(00\bar{1})$, where the minus sign (bar) above the relevant index represent the negative intercepts. The perpendicular distance between two parallel planes (hkl) can be calculated by:

$$d = \frac{1}{[(h/a)^2+(k/b)^2+(l/c)^2]^{1/2}} \tag{2.3}$$

Combined with the X-ray diffraction result, the materials' property and structure information can be extracted, which will be discussed in section 2.3.

Directions in the crystal are determined by the perpendicular planes. Generally, the direction perpendicular to the plane (hkl) is [hkl], enclosed in square brackets. The angular bracket notation <hkl> is used to describe a complete set of equivalent directions.

2.2.2 Epitaxy growth and strain

Generally, epitaxy is a growth process of a solid film on a crystalline substrate in which the atoms of the growing film are in some registry with respect to the atoms of the substrate. The similar crystal structure and similar orientation as the substrate is highly expected for the epitaxial growth, such as the GaAs/AlGaAs material system growth, which is commonly used in THz-QCL structure [27]. However, there are also many cases, typically as the requirement

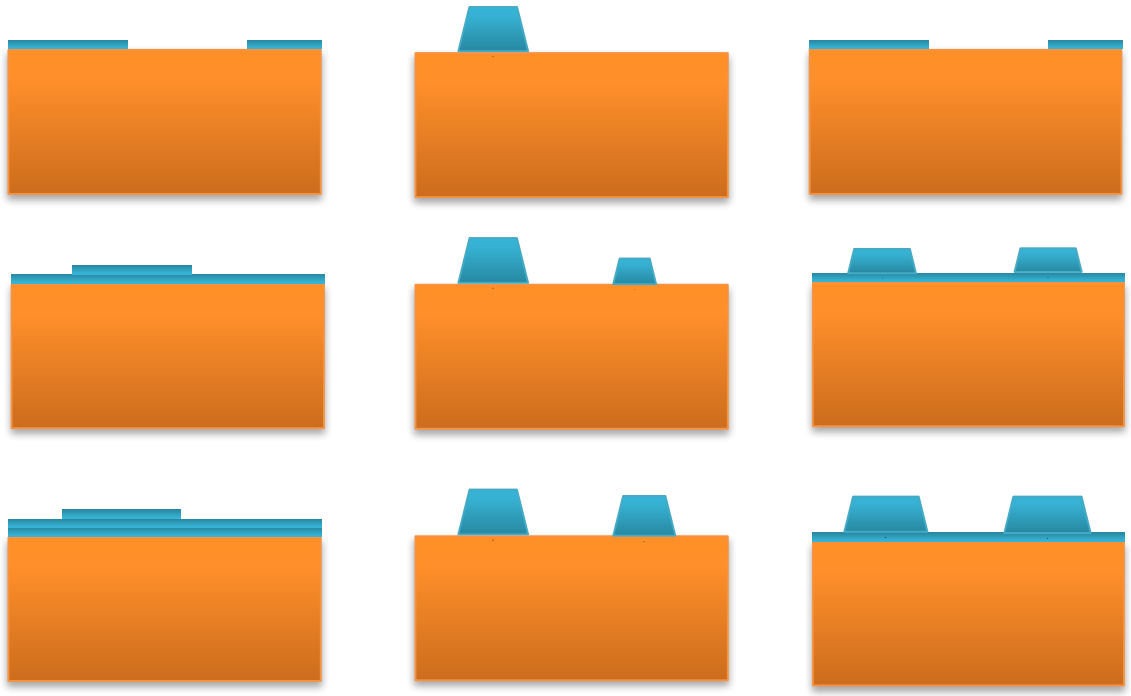

Figure 2.4: The three main modes of epitaxial growth, Layer-by-layer or Frank-van der Merwe growth (a), island or Volmer-Weber growth (b), and layer plus island or Stranski-Krastanov growth (c).

of specific device design, where the epitaxial layer is mismatched with the substrate. For example, AlGaN/GaN heterostructures grow on Si (111) substrate [28].

There are three main modes of crystal growth, distinguished depending on the relative bond strengths between source atoms and substrate, as shown in Figure 2.4. Firstly, the layer-by-layer, also called as Frank-van der Merwe mode, is illustrated in Figure 2.4 (a). As a result of the bond between the source atoms and the substrate being stronger than to each other, the v atoms are more likely to form a complete monolayer before starting the next. Secondly, if the source atoms are bound weaker to the substrate than to each other, the very first atoms tend to aggregate instead of forming a complete layer. Therefore, islands shape of epitaxial materials is nucleated on the substrate surface, which is known as island growth. Finally, as the "intermediate" case between the above two growth type, layer plus island, also called as

Stranski-Krastanov growth, is defined. It is usually observed in small misfit epi-layer growth. After forming the first or several monolayers, the homogeneous strain energy ϵ_H becomes so large that a thickness is reached where coherent interface forming becomes energetically unfavorable [29]. This thickness is described as the critical layer thickness for 2D-3D transition. As the epi-layer thickness keeps increasing, three dimensional structure as the islands are formed on top the so-called "wetting" layer.

If the lattice constant misfit between the substrate and the epi-layer is sufficiently small, either compressive (epi-layer lattice constant is larger than the substrate lattice constant) or tensile (epi-layer lattice constant is smaller than the substrate lattice constant) strain is formed, which is defined as:

$$\varepsilon = \frac{\delta d}{d_0} = \frac{d - d_0}{d_0} \tag{2.4}$$

where *d* and d_0 are the lattice constant of the strained and relaxed layer, respectively.

In a fully strained model, the strain along the growth direction is calculated as

$$\varepsilon_z = -\left(\varepsilon_x + \varepsilon_y\right)\left\{\frac{v}{1-v}\right\} \tag{2.5}$$

where v is the Poisson ratio. By replacing the strain values along the three orthogonal directions with $\varepsilon_z = \frac{a_L^{\perp} - a_L}{a_L}$, $\varepsilon_x = \varepsilon_y = \frac{a_s - a_L}{a_L}$, the vertical lattice constant of the epi-layer $a_L^{\perp}$ can be derived as

$$a_L^{\perp} = a_L \frac{1+v}{1-v} - a_s \frac{2v}{1-v} \tag{2.6}$$

where a_s and a_L are the lattice constant of the substrate and the unstrained epi-layer, respectively. Vertical lattice constants for several materials on InAs substrates are calculated and listed in table 2.1.

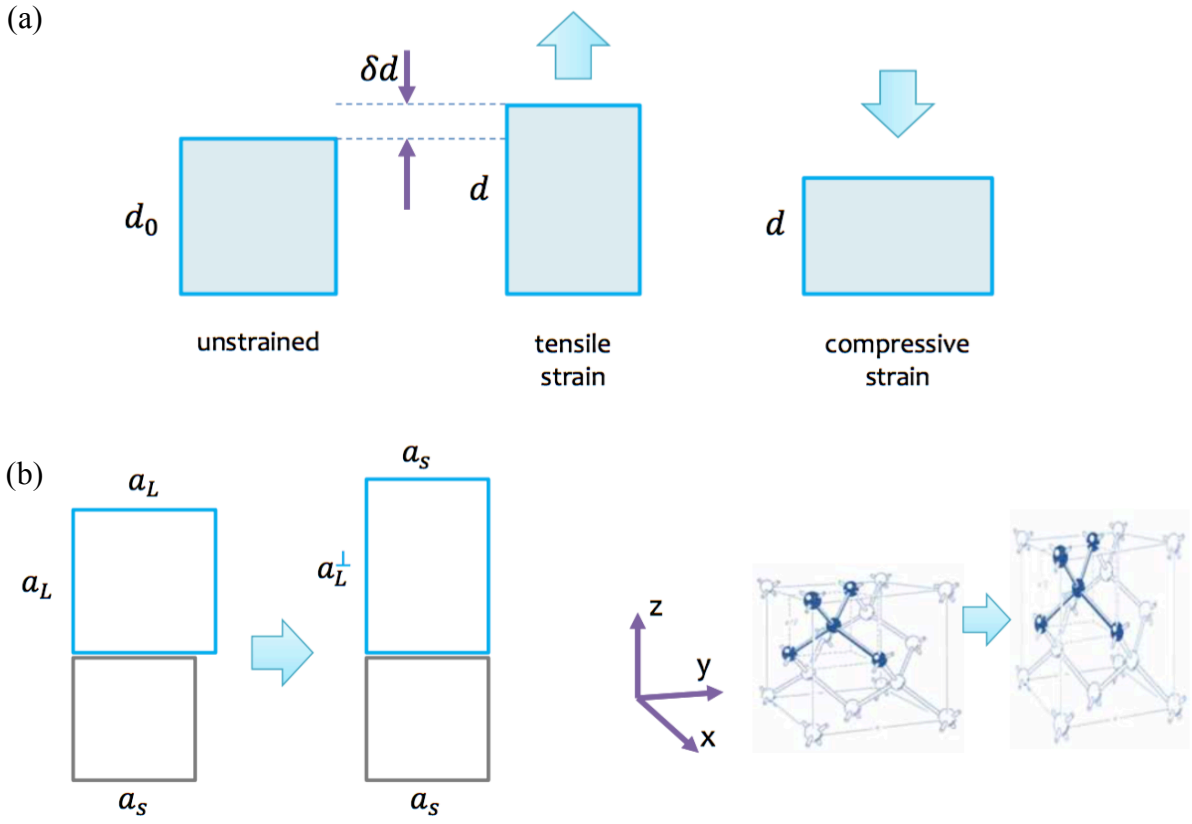

Figure 2.5: Schematic view of tensile and compressive strain (a), and a fully strained model (b) [31].

Table 2.1: Material vertical lattice constant on InAs substrate.

Material	Lattice constant (Å)	Poisson Ratio v	$a_L^{\perp}$ on InAs substrate
InAs	6.05840	0.352	6.05840
AlSb	6.13550	0.317	6.20707
AlAs (Ref [30])	5.66143	0.325	5.27916
InSb	6.47880	0.353	6.93754

2.3 X-ray diffraction

X-ray diffraction is a rapid analytical method of investigating the fine structure of a crystal. The first experiment of studying the materials by diffraction is performed by Laue, Friendrich and Knipping in 1911 [32]. With the development of both experimental and theoretical tools, nowadays, not only the epi-layers structures but also the composition of a ternary compound or the stress in heteroepitaxial films can be determined by this method [33-34].

2.3.1 Bragg's law and X-rays

Diffraction is essentially due to the existence of certain phase relations. It is well known that two rays are completely in phase whenever their path lengths differ by either zero or a whole number of wavelengths.

This condition for efficient specular reflection is called Bragg's law (as shown in Figure 2.6):

$$2dsin\theta = n\lambda \tag{2.7}$$

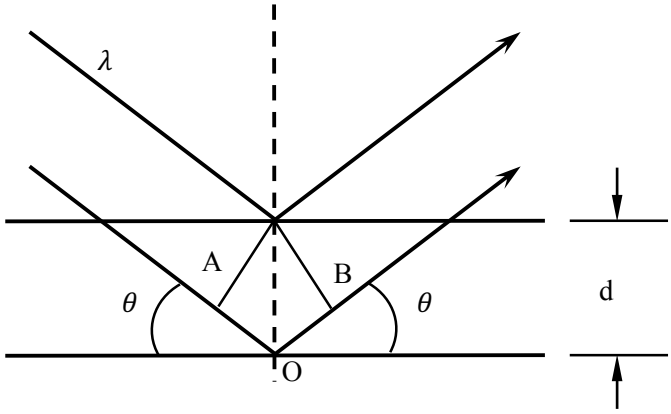

Figure 2.6: Bragg diffraction. Two parallel beams with identical wavelength and phase are shown, scattered by two parallel atomic planes with the separation distance of *d*. Strong diffraction is observed, when the angles of incidence and diffraction θ are equal, and the path difference AOB between the two beams is equal to $n\lambda$, which is an integral number of wavelengths.

where d is the distance between the lattice planes, θ_B the so-called Bragg angle, which is measured between the direction of the incident beam and the lattice plane under consideration, and n is an integer. On one hand, derived by that equation, the basic condition $n\lambda < 2d$ must be satisfied to obtain each diffraction as a result of the term $sin\theta$ cannot exceed 1. Since the distance between two planes is of the order of 3 Å, the choice of λ should be lower than 6 Å. Typically, the Cu Kα_1 radiation ($\lambda = 1.540$ Å) is chosen as the high resolution XRD source wavelength.

2.3.2 Superlattices

The theory in this subsection is taken from subsection 4.7.3 in Semiconductor Science, written by Tudor E. Jenkins [35].

Superlattices are the structures with two (or more) materials are periodically repeated and the thickness of each layer is typically at several nanometers range. They will exhibit a periodicity corresponding to the lattice periodicity in X-ray diffraction patterns. The model superlattices consist of two different materials (A, B), in the sequence ABABAB…, is introduced in this section. With the combination of layer thickness D_A and D_B, a new periodicity D along the growth direction is formed, as shown in Figure 2.7.

$$D = D_A + D_B \tag{2.8}$$

Considering the conventional unit cell along the horizontal plane and the unit cell of the superlattice as one period AB of the superlattice in the growth direction, diffraction patterns are obtained due to the superlattice periodicity superimposed on the diffraction patterns, by providing the comparable X-rays wavelength. Recall the function

$$2Dsin\theta = L\lambda \tag{2.9}$$

where L is an integer. At angles θ, the superlattice peaks are observed. The intensity of these peaks is determined by the structure factor of the AB layer. We can consider the superlattice is consist of n_{InAs} monolayers of InAs and n_{AlSb} monolayers of AlSb. In a fully strained model,

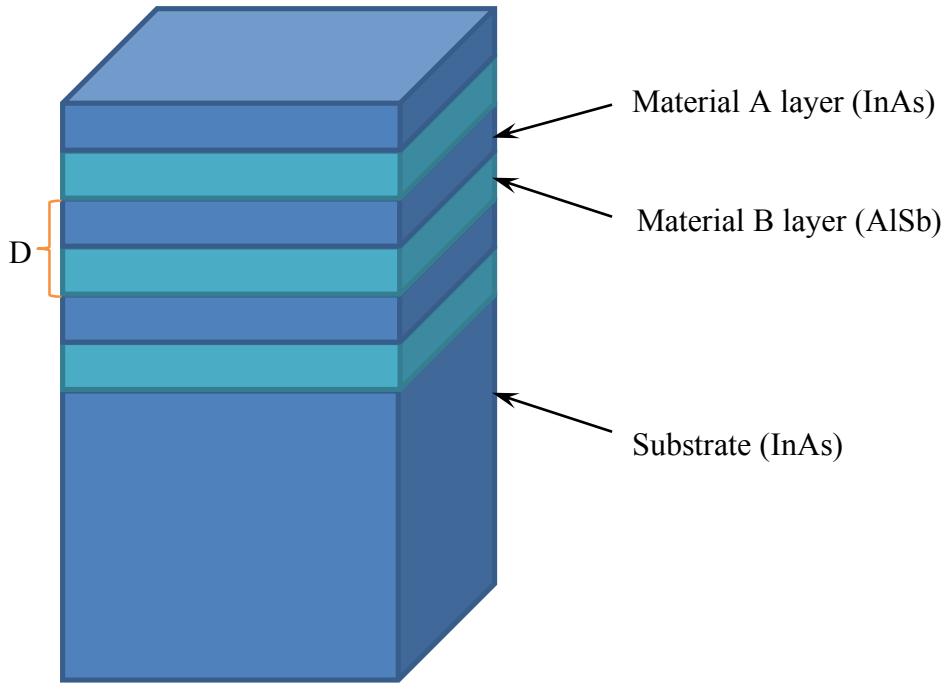

Figure 2.7: Superlattice configuration consists of material A (InAs) and material B (AlSb).

assuming the superlattice growth direction coincides with the (100) axes of the crystal, one monolayer equals half of the vertical lattice constant of the InAs and AlSb. We can write

$$D_{\mathrm{InAs}} = \frac{n_{\mathrm{InAs}} a^{\perp}_{\mathrm{InAs}}}{2} \tag{2.10}$$

$$D_{\mathrm{AlSb}} = \frac{n_{\mathrm{AlSb}} a^{\perp}_{\mathrm{AlSb}}}{2} \tag{2.11}$$

where a_{InAs} and a_{AlSb} are the lattice constant of InAs and AlSb, respectively. Bragg reflection occur at angles

$$sin\theta = \frac{L\lambda}{n_{\mathrm{InAs}} a^{\perp}_{\mathrm{InAs}} + n_{\mathrm{AlSb}} a^{\perp}_{\mathrm{AlSb}}} \tag{2.12}$$

When $L = \frac{l}{2}(n_{\mathrm{InAs}} + n_{\mathrm{AlSb}})$, where l is an integer

$$sin\theta = \frac{(n_{\mathrm{InAs}} + n_{\mathrm{AlSb}})l\lambda}{2(n_{\mathrm{InAs}} a^{\perp}_{\mathrm{InAs}} + n_{\mathrm{AlSb}} a^{\perp}_{\mathrm{AlSb}})} \tag{2.13}$$

As a result of the superlattice is grown on InAs, the InAs vertical lattice constant $a^{\perp}_{\mathrm{InAs}} = a_{\mathrm{InAs}}$. Hence, equation 2.13 is deduced as $sin\theta = \frac{(n_{\mathrm{InAs}}+n_{\mathrm{AlSb}})l\lambda}{2(n_{\mathrm{InAs}}a_{\mathrm{InAs}}+n_{\mathrm{AlSb}}a^{\perp}_{\mathrm{AlSb}})}$. Recall the average lattice constant of the superlattice $\langle a\rangle = \frac{n_{\mathrm{InAs}}a_{\mathrm{InAs}}+n_{\mathrm{AlSb}}a^{\perp}_{\mathrm{AlSb}}}{n_{\mathrm{InAs}}+n_{\mathrm{AlSb}}}$, the Bragg formula for scattering from a crystal of lattice constant $\langle a\rangle$ is reduced to

$$sin\theta = \frac{l\lambda}{2\langle a\rangle} \tag{2.14}$$

This superlattice diffraction peak is called the zero-order peak which is located somewhere between the Bragg reflection peak of material InAs and AlSb. The superlattice peaks around it are called satellites, with indices ±1, ±2, ±3, etc.

In terms of the angular peaks separation between satellite peaks and the zero-order peak, we can write the Bragg equation as

$$2Dsin\left(\theta_p + \theta_B\right) = m\lambda \tag{2.15}$$

where θ_p is the angular separation between order m superlattice satellite and the zero-order superlattice peak, which is given by $sin\theta_B = \frac{(n_{\mathrm{InAs}}+n_{\mathrm{AlSb}})l\lambda}{2(n_{\mathrm{InAs}}a_{\mathrm{InAs}}+n_{\mathrm{AlSb}}a^{\perp}_{\mathrm{AlSb}})}$.

For two superlattice orders p, q

$$2D\left[sin\left(\theta_p + \theta_B\right) - sin\left(\theta_q + \theta_B\right)\right] = (p-q)\lambda \tag{2.16}$$

As θ_p and θ_q are small (typically at milliradians range), then $sin\theta_{p,q} \approx \theta_{p,q}$ and $cos\theta_{p,q} \approx 1$. Therefore,

$$2D\left[\theta_p cos\theta_B - \theta_q cos\theta_B\right] = (p-q)\lambda \tag{2.17}$$

$$D = \frac{(p-q)\lambda}{\Delta\theta_{p,q} cos\theta_B} \tag{2.18}$$

where $\Delta\theta_{p,q} = \theta_p - \theta_q$ is the angular separation of two satellites p and q.

Chapter 3

Experimental Methodology

3.1 Molecular beam epitaxy

3.1.1 MBE components

Typically, modern machines have a modular design, in order to achieve a definite process for each module. Four types of modules may be included on the system: load-lock, preparation, cluster, and growth module, as shown in Figure 3.1. All of those chambers, where the wafers are introduced in and extracted, are individually pumped and kept under ultra-high vacuum (UHV), except load-lock module (easier for wafer introducing and extracting). As a result of the specific variant of MBE machines developed for different purpose, such as research or production, the materials to be grown, the layouts of MBE machines may be different. For here, we introduce the configuration of the MBE system used for this work-Veeco GEN10. It contains a growth chamber fit with different real-time analytical techniques; a cluster tool chamber for wafer storing; a preparation chamber for in-situ cleaning and a load-lock chamber for loading and unloading the wafers.

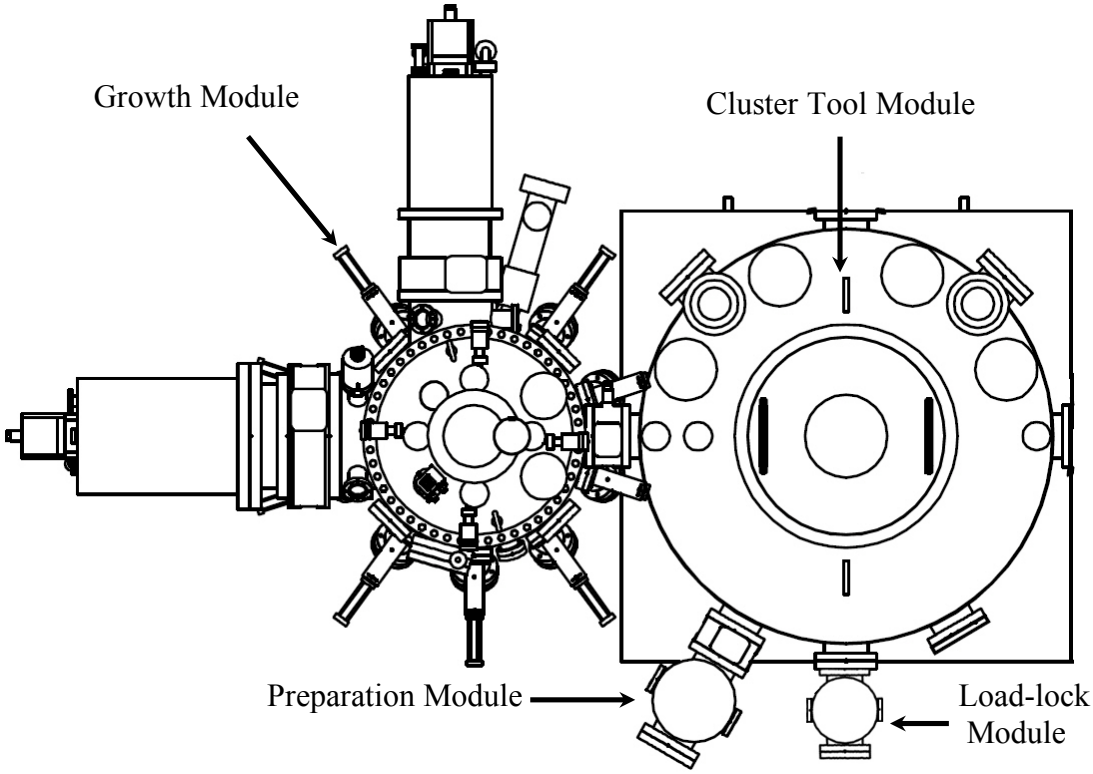

Figure 3.1: Schematic view of a modular designed MBE system [36].

Load-lock module

Load-lock module is designed for manual loading of wafers into the system, and removal of wafers after processing. It contains a load-lock elevator structure which moves the lock-lock shelf assembly up and down inside the module. It allows the robot and operator to access different shelves during loading or removal of platens. The load-lock module is directly connected to the cluster module with a gate valve. After exposure to ambient while loading and unloading wafers, the load lock is pumped down with a turbo molecular pump while simultaneously heated up to 200°C. After about 2 hours the pressure inside the load-lock module reaches low 10^{-8} Torr, at which point the gate valve to the cluster tool can be opened for the transfer of the new wafers and for removal of grown layers without breaking UHV.

Preparation module

The preparation module is where substrates are conditioned through high-temperature outgassing and optionally hydrogen plasma cleaning before transfer to the growth module for epitaxial growth.

Cluster tool module

Serving as the hub for module-to-module transfers, cluster tool module houses a robot which transfers platens from module to module. Other modules surround the cluster tool module in a "satellite" configuration. It also includes two storage shelf assemblies than can hold up to 16 platens with wafers.

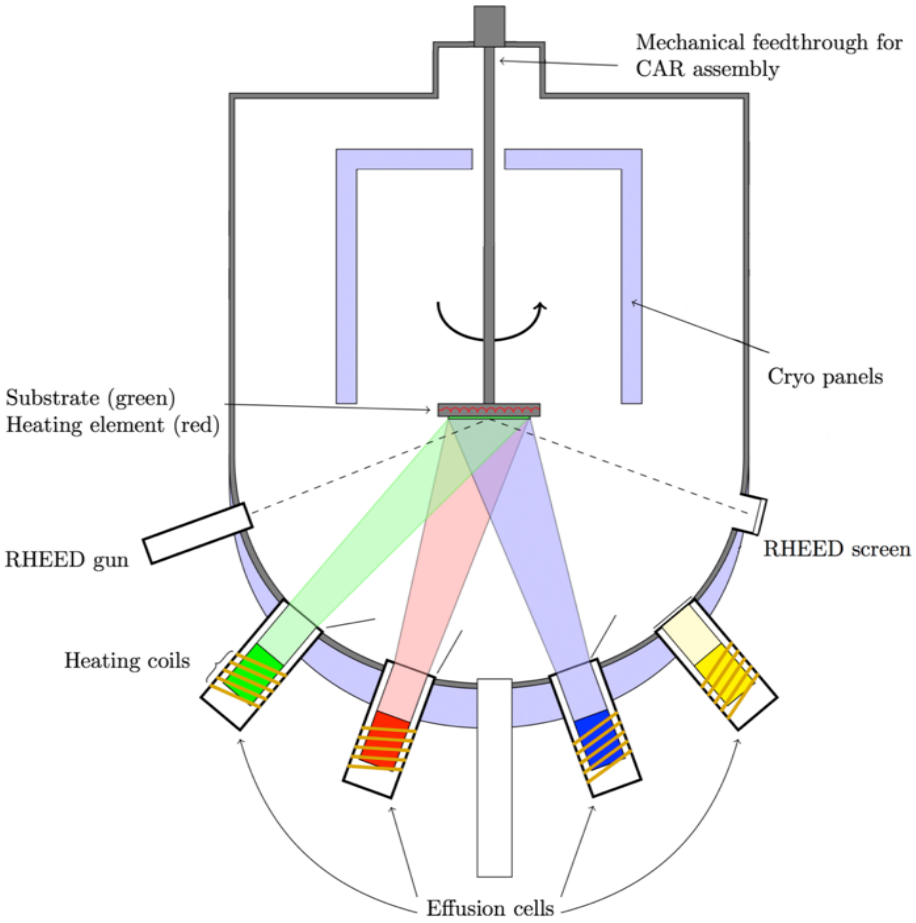

Figure 3.2: Schematic view of MBE growth chamber [37].

Growth module

Growth module (Figure 3.2), as the location for epitaxial growth, contains a stainless steel vessel; source ports for material-specific MBE cells; a vertically mounted substrate manipulator with integral heater and rotating growth stage; an internal cryopanel that contains a cooling liquid (typically liquid nitrogen) to condense water vapor and other undesired gas species. Growth module accommodates a CT10 cyropump, an ion pump, vacuum gauges, analytical instruments, and in-situ monitoring equipment, depending on the system configuration.

In order to limit the incorporation of contaminants which may affect material quality and morphology, the chambers are evacuated to base pressures of a few 10^{-11} Torr. Two parameters, closely related to pressure, which are important for the characterization of vacuum, are the mean free path and the concentration of the gas molecules penetrating the vacuum [38]. Mean free path is defined as the average distance traversed by the molecules between successive collisions. According to the ordinary assumptions of the kinetic theory of an ideal gas, the mean free path is given by [39-40]:

$$L = \frac{1}{\sqrt{2}\pi n d^2} \tag{3.1}$$

where d is the molecular diameter, and n is the concentration of the gas molecules which depends on the pressure p and the temperature T:

$$n = \frac{p}{k_B T} \tag{3.2}$$

where k_B is the Boltzmann constant 1.381×10^{-23} JK^{-1}. Substituting this expression into (1), the mean free path of the gas molecules is obtained (in SI units):

$$L = 3.11\times10^{-24}\frac{T}{pd^2} \tag{3.3}$$

For instance, the mean free path of a Ga molecular ($d_{Ga} = 3.74$ Å) under a pressure of 10^{-5} mbar and at 300 K, is approximately 7 m. The molecular beams, generated in effusion cells, in a typical MBE reaction chambers, traverse a distance approximately equal to 0.2 m between the substrate and the outlet orifices of the beam sources, thus virtually all atoms and molecules

reach the substrate in straight paths without undergoing collisions. The detailed calculations of the molecular flux geometry and their influence on the uniformity of the growth layers can be found in Ref. [41]

3.1.2 In-situ characterization tools

UHV environment of MBE enables real-time monitoring of growth process with a number of in-situ monitoring tools. With the development of multi-chamber MBE system, many other surface diagnostic facilities have been incorporated. For example, AES (Auger electron spectroscopy), used for the determination of the surface chemical composition of the or bulk chemical composition of the grown layers with the depth profiling procedure; X-ray photoelectron spectroscopy (XPS) [42], for studying the electronic structure of the epi-layer surface; Secondary ion mass spectroscopy (SIMS) [43], mainly for determining of the chemical composition of the outermost epi-layer of the grown structure. Those analytical techniques are post-growth in-situ techniques providing important information about the films or surfaces grown without undesirable exposure to atmosphere. Below, the in-situ characterization tools which were used in this project are reviewed.

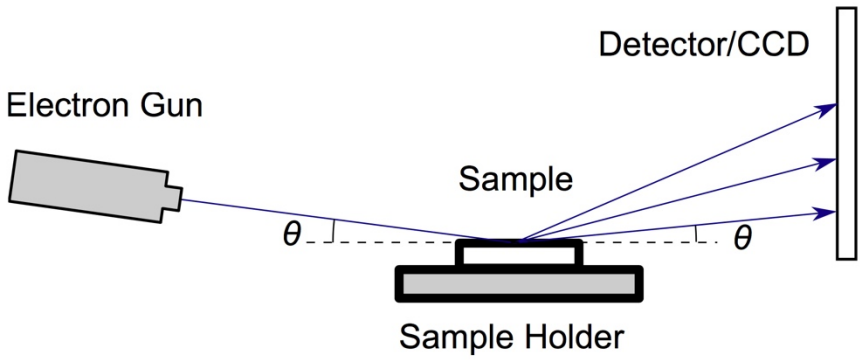

Figure 3.3: Schematic setup of RHEED which consists of the electron gun, sample and fluorescent screen and CCD camera. Electrons generated by the electron gun strike the sample with an incident angle θ. Diffracted by the atoms on the sample surface, the electrons reach to the phosphorous coated screen and form the RHEED pattern [44].

Reflection high-energy electron diffraction - RHEED

RHEED is one of the most effective in-situ characterization tools used for studying the growth kinetics and surface reconstruction. It also gives early warning signs if the epitaxial growth is not progressing properly. Typically, a high energy beam of electrons, in the range of 5-40 keV, is directed at a low angle to the sample's surface (Fig. 3.3). Because of the low incident beam angle, typically at 1º- 3º, the penetration of the surface by electrons is restricted to the couple of outermost atomic layers.

Flux monitoring ion gauge

Most MBE applications necessitate excellent control over atomic fluxes to obtain highly accurate layer thicknesses and compositions for ternary and quaternary compounds. The most widely used method for measuring beam fluxes is based on the use of a movable ion gauge, which can be placed between the effusion cell and the substrate to measure the atomic flux before the growth (beam equivalent pressure, BEP). This is not an absolute measurement method, but can be accurately calibrated for each effusion cell using other in-situ or ex-situ techniques.

Monitoring of residual gases

In MBE system, simple and reliable gas analytical equipment is highly desired for the residual gas detection. Bayard-Alpert gauges are used for all routine vacuum monitoring. This is important for maintaining adequate vacuum quality. The pressure monitored by these gauges also provides a "figure of merit" with which to check vacuum integrity on a day-to-day basis.

Another commonly used gas monitoring tool is the residual gas analyzer (RGA) [45-46]. The residual gas spectrum produced by RGA is very useful for warning about small leaks from ambient or presence of some undesirable species in the UHV environment. In the event of detection of traces of air in the system, RGA is the key tool to pinpoint the location of the leak. For that, helium gas is directed to the different points on the exterior of the system components, while the presence of He atoms inside the UHV is being monitored.

Band-edge thermometry (BET) and integrated spectral pyrometry (ISP)

Band-edge thermometry, also known as absorption band-edge spectroscopy (ABES), is often used for the substrate temperature monitoring. Generally, the absorption spectrum of a semiconductor can be used as a temperature indicator. The bandgap of a semiconductor (E_g) is temperature dependent and this dependence can be described by the Varshni empirical expression:

$$E_g(T) = E_g(0) - \alpha \times \frac{T^2}{T+\beta} \tag{3.4}$$

where α and β are two material dependent coefficients. BET works by detecting the absorption edge position and its shifts as a function of temperature. However, it can be used reliably only for certain class of substrates, such as undoped GaAs or InP. The source of light could be either the heater itself, or a halogen lamp radiation delivered by a quartz light-pipe to the back of the wafer for low temperature growth. Unfortunately, this method is not suitable for narrow-gap materials, such as InAs. For the growth on InAs substrates the temperature was measured using the same InGaAs array spectrometer normally used for BET, but in this case rather than analyzing the light transmitted through substrate, the intensity of the thermal radiation from the wafer was collected from about 10 mm diameter spot at the wafer center and integrated over the spectral range from 900 to 1700 nm. In this spectral range InAs is opaque, so only the thermal emission is responsible for the measured signal. This new temperature monitoring method will be further referred to as the Integrated Spectral Pyrometry, or ISP for short. Procedure for calibration of such thermal emission versus InAs wafer temperature goes beyond the scope of this thesis is described elsewhere (M. C. Tam, D. Gosselink, Y. Shi, M. Jaikissoon, Z. R. Wasilewski, Journal of Vacuum Science and Technology, to be published).

3.2 Ex-situ characterization tools

For further characterization of the material properties such as the carrier concentration, compensation and the actual layer thickness detection, the post-growth or ex-situ

characterization tools are required. For instance, structure related properties such as the strains or layer thicknesses can be detected by XRD [47], electrical properties such as the carrier density and mobility can be measured using Hall effect [48]. The range of ex-situ characterization tools is very large. In this subsection, the ex-situ characterization tools used in this work, HRXRD and Nomarski differential interference contrast (DIC) microscopy, will be discussed.

3.2.1 High resolution X-ray diffraction

High resolution XRD is an instrument which is typically used in evaluation of epitaxy growth structures. It has been employed in the metrology of compound semiconductors since about 1980, and greatly helped in establishing and control of the compositions and thicknesses of epitaxial structures.

As shown in Figure 3.4, a high resolution XRD triple-axis instrument is comprised of an X-ray source, a beam conditioner, a sample stage to manipulate the specimen, an analyzer crystal and a detector. Typically, X-ray is generated by electrons bombarding a copper target under 40 kV bias. Since the output spectrum spreads over a large wavelength range, a beam conditioner is used to collimate and monochromate the beam to satisfy the requirement of high angular resolution and sufficient monochromatization. The CuKα_1 line ($\omega = 1.54056$ Å) is the most popular choice as its high intensity and convenient operation for laboratory use. The analyser crystal, fixed in front of the detector, allows to upgrade the scanning mode from double-axis to triple-axis. In a double-axis mode, the analyser crystal or a detector slit is removed, and the signal collected by the detector is the integration of the beams scattered from the sample over a range of angels which are limited only by the detector aperture. If significant strain-induced curvature of the wafer is present, or the layers contain structural defects, some important information may be lost or blurred. In a triple-axis geometry, by adding an analyzer crystal between specimen and the detector, one can perform more advanced analysis separating the effects of sample curvature or tilts of mosaic spread from elastic strain effect, particularly if diffractograms are collected using both symmetrical and asymmetrical Bragg reflections.

HRXRD measures the intensity distribution with respect to the ω (angle between specimen and incident beam), 2θ (angle between the incident beam and detector angle), or both of them, which can result in three XRD scan types: Rocking Curve scan, Detector Scan and Coupled Scan, respectively. Typically, the incident beam direction is fixed for all these scan types. In a rocking curve scan, the detector position is also fixed, while the sample is rotated around the omega-axis. It is mainly used for the defects study such as the dislocation density and the wafer curvature. In terms of the detector scan, the orientation of specimen is fixed. X-ray intensity verifies as the detector rotates along the 2θ-axis. The plot of the scattered X-ray intensity as a

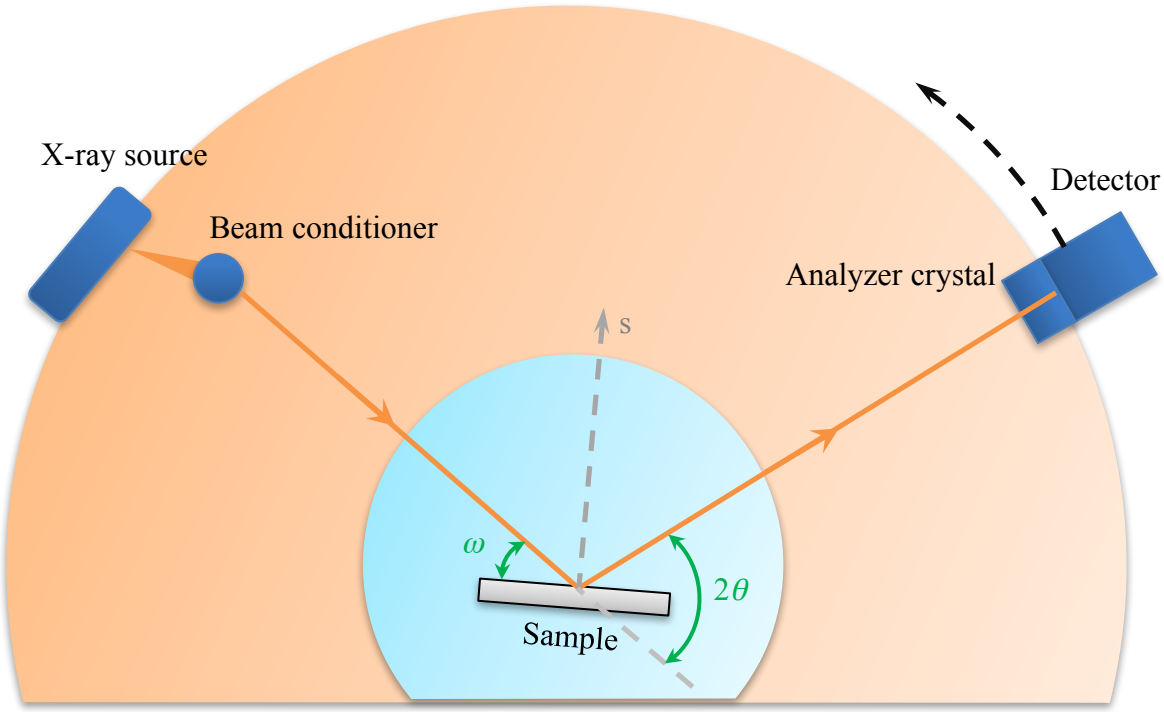

Figure 3.4: Schematic of high resolution X-ray diffraction triple-axis setup.

function of 2θ, while the sample orientation also changes with $\omega = {}^{1}/_{2} \times 2\theta + offset$, is called coupled scan. The lattice mismatch, relaxation, thickness and superlattice period information can be investigated by this scanning type, which is primarily used in this project.

The HRXRD instrument used in this project is a QC3 manufactured by Jordan Valley Semiconductors Ltd. The measurement results analysis is based on Jordan Valley Rocking-Curve Analysis by Dynamical Simulation (RADS) version 5.2.22.

3.2.2 Differential interference contrast (DIC) or Nomarski microscopy

Differential interference contrast microscopy, also known as Nomarski microscopy, is generally used for the planar semiconductor processing analysis or live and unstained biological samples imaging. Thanks to sophisticated combination of polarizers and birefringent crystal prisms, the contrast is related to the gradient of optical paths in the observed specimen. In the case of the reflecting geometry used for the semiconductor wafer inspection DIC image is a close representation of the surface morphology with extremely high vertical resolution approaching 1nm. Therefore, Nomarski microscopy is considered as one of the best first-line tools for rapid evaluation of wafer surface defects.

3.3 Experimental procedure

3.3.1 Growth recipe

The substrates used in this project are 2 inch sulphur doped InAs with the surface orientation of (100), produced by Wafer Technology Ltd. Most of the wafers are cleaved into quarters for calibration growth and growth optimization. Before being transferred into the growth chamber, the substrate, mounted with the retainer and spring within a wafer holder, needs to be pre-outgassed at 200 °C in the Load-lock (LL) chamber for 2 h. When the chamber cools down and the pressure in the LL reaches low 10^{-8} Torr level, the whole set is transferred to the Preparation Module (PM) for further outgassing before transferring to the growth module for an epitaxial growth.

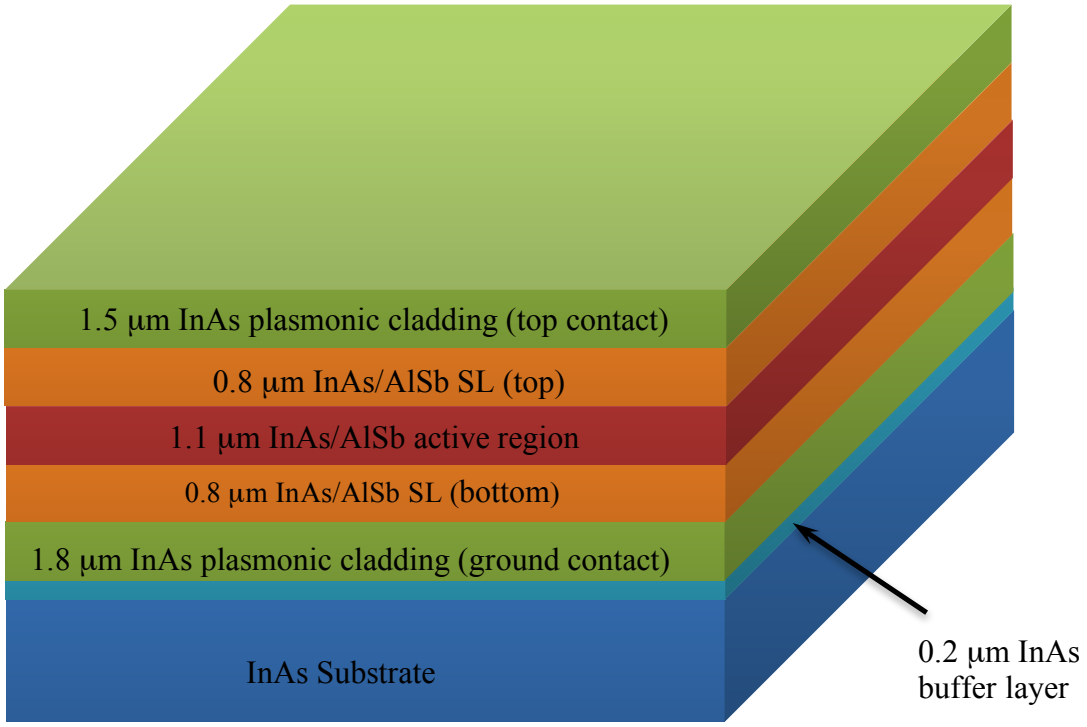

Figure 3.5: Schematic view of a QCL bare wafer.

The full structure growth recipe starts with oxide layer desorption. For that, the InAs substrate is annealed at 540 °C for 10 min under As flux to prevent InAs decomposition. Figure 3.5 shows the layer structure of the QCL devices that were grown in this study. Two different growth recipes had been tested for the 0.2 μm InAs buffer layer, with the details discussed in Chapter 4. The 1.8 μm highly doped InAs plasmonic cladding layer and the following layers were grown at 420 °C. The substrate temperature was monitored by the ISP method described in section 3.1.2, while the manipulator thermocouple, located between the heater and the substrate provided the reference signal to the PID controller stabilizing substrate temperature. Typically, the growth rate was 2.78 Å/s for the InAs buffer layer, the bottom and top plasmonic cladding layer. The growth rate was 1 Å/s for the InAs and AlSb layers in both SL spacer regions and the active layer.

3.3.2 Device fabrication

Laser devices with a disk mesa or ridge waveguide have been fabricated out of the grown wafers. Fig. 3.6 shows a schematic diagram of a disk laser device (a) and the cross-section diagram of a ridge waveguide laser device (b).

Standard photolithograph is employed for the device fabrication. In a disk device, a round mesa is dry etched through the epi-layers down to the InAs substrate (Fig. 3.6 (a)). A thin gold layer, used for top contact electrode, is deposited onto the top of the mesa. A disk-mesa laser device is easy to be fabricated, however, the device performance is not optimized. The fabricated disk devices are mainly for the purpose of proof-of-concept.

The fabrication process for ridge waveguide devices is more complicated, as shown in figure 3.6 (b). The whole process includes four rounds of photolithography. The overall procedure are as follows:

a. Define the top contact metal Au/Ti by photolithography.

b. Deposit SiN_x layer by PECVD (plasma enhanced vapor deposition).

c. Another photolithography for ridge patterning. Then use reactive ion etch (RIE) to define the ridge waveguide.

d. Back side metal deposition for a better ohmic contact with negligible contact resistance.

e. Deposit ~550 nm SiN_x for passivation, etch grooves to electrically isolate neighboring devices.

f. Pattern the contact hole by the third round of photolithography, and deposit the top metal seed layer Au/Ti.

g. The last round of photolithography for the isolation etch of the top spread metal layer.

The fabricated device die is then cleaved to individual laser bars (1cm x 1mm), and mounted to a copper package with indium soldering which is also used for the accommodation of the large thermal expansion mismatch between the InAs substrate and copper package. After wire-

bonding individual laser devices, the fabricated QCL are ready for electrical and optical characterizations.

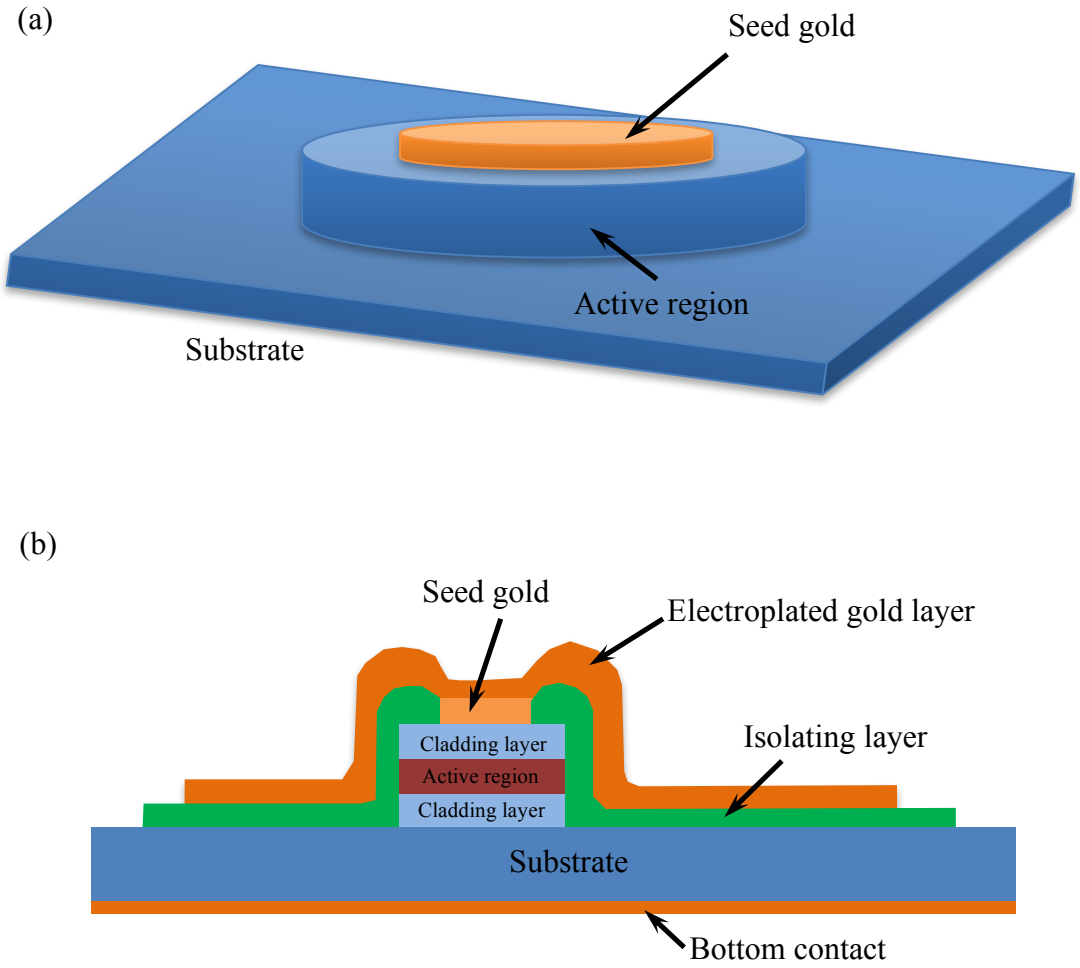

Figure 3.6: (a) Schematic view of a disk mesa waveguide QCL device; (b) cross section view of a ridge waveguide QCL device.

3.3.3 Light-current-voltage measurement

Figure 3.7 shows the experimental set-up used for the light-current-voltage (L-I-V) measurement. For most devices, in order to reduce the self-heating effect from the characteristics, the characterization is generally performed in pulsed mode and the duty cycle is generally limited to 1-2%.

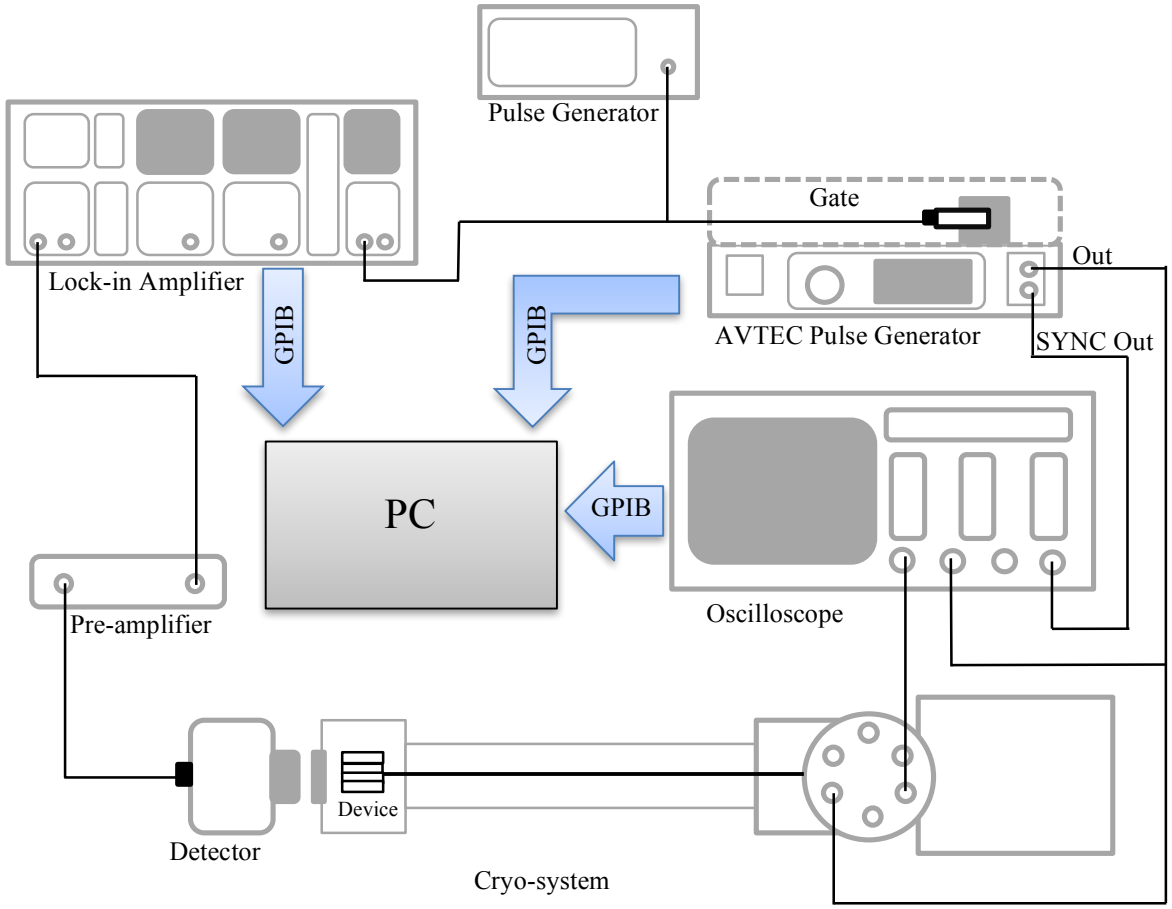

Figure 3.7: Schematic drawing of the pulse mode L-I-V measurement set-up. The device is mounted on a continuous He-flow cryostat. The bias is supplied by a AVTEC pulse generator. Both of the current and voltage information is measured and recorded by the oscilloscope. The detector is placed directly facing the device and connected to a pre-amplifier. Adding a lock-in amplifier followed by the pre-amplifier, the light power can be quantitatively measured.

The bias is supplied by a pulse generator (made by AVTEC Inc.). The current is directed measured by a current probe, directly connected to the pulse generator output port, while the voltage is measured through a high-impedance input oscilloscope. As a result of the resistance of the device (QCL) changes under different applied bias or different temperature, an inner circuit is designed for the device connection in order to achieve a better impedance match (~50 Ω). The device is mounted in a cryostat, which enables the temperature tuning from 10K to room temperature.

In terms of the optical power measurement part, another pulse generator is connected to the system. It generates a 20 Hz signal, which is used as the reference in lock-in amplifier. The optical power is collected by a Mercury Cadmium Telluride detector (2 to 26 μm) and transferred to the electrical signal. It is further amplified by a pre-amplifier and finally recorded by the lock-in amplifier.

Chapter 4

Results and Discussion

4.1 Growth result

In this section, both of the MBE related growth results and part of the device characterization results are discussed. The XRD characterization, is discussed separately in section 4.2. Below, the buffer layer and bottom cladding layer optimization growth results are discussed. With key growth parameters calibrated by this first step, the full structure growth is tested, and the results are discussed in the second subsection. Followed by the fabrication process which is performed in University of Waterloo's Quantum NanoFab, both of the LIV and FTIR tests are employed for the device performance characterization, and the results are shown in the last subsection.

4.1.1 Buffer layer and bottom cladding layer growth

As designed, the MIR-QCL active region with the SL spacers were grown on an n-InAs (100) substrate on which a 2000 Å InAs buffer layer and a 1.8 μm highly doped bottom cladding layers were grown first. In order to obtain a high quality morphology of a full structure growth, the growth condition of buffer layer and bottom cladding layer needed to be optimized. Four growths (Sample A, Sample B, Sample C and Sample D) were prepared for the growth condition optimization, where the first three growths were focused on the buffer layer optimization and Sample D incorporated both, the buffer layer and cladding layer.

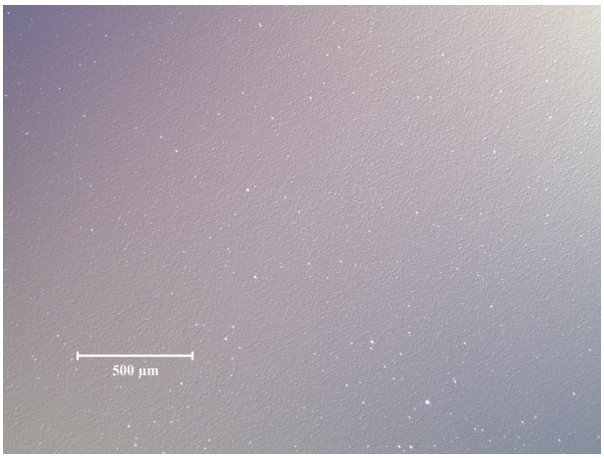

(a) ×50 magnification

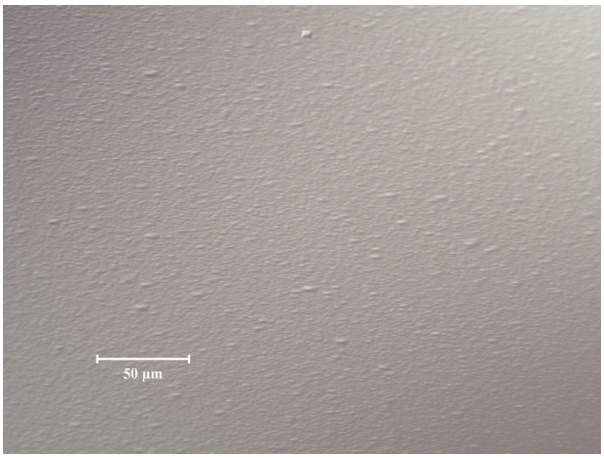

(b) ×400 magnification

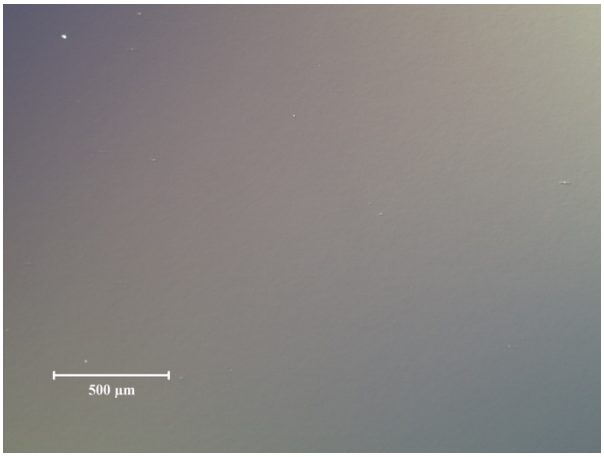

(c) ×50 magnification

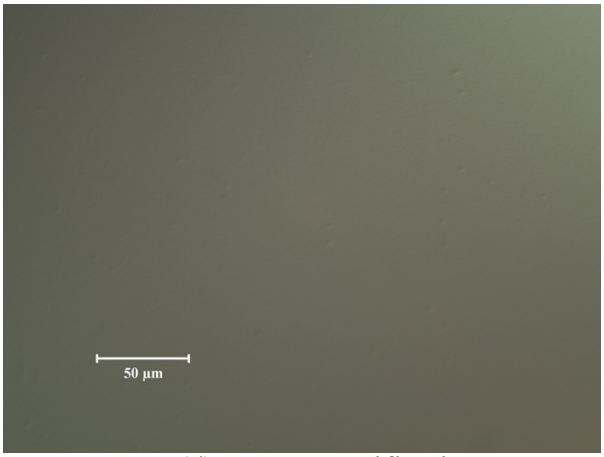

(d) ×400 magnification

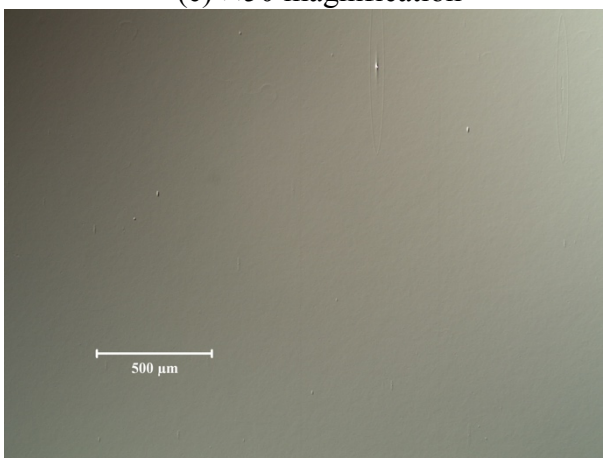

(e) ×50 magnification

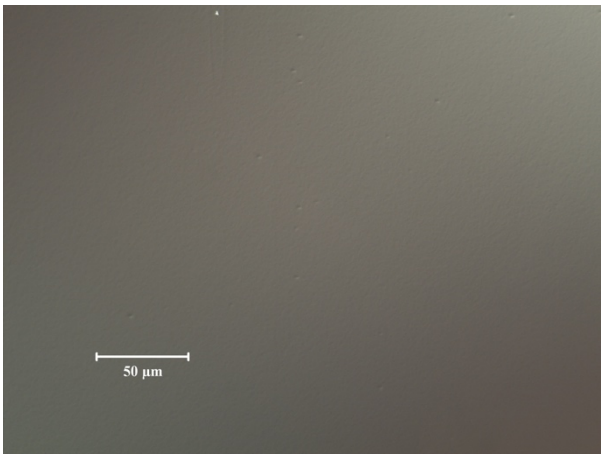

(f) ×400 magnification

Figure 4.1: Nomarski images for Sample A (a), (b); Sample B (c), (d); Sample C (e), (f).

The detailed growth conditions are as follows:

Sample A: Ramp substrate temperature to 550 °C anneal for 10 min, then cool down to 520°C for the 2000 Å InAs buffer layer growth.

Sample B: Ramp substrate temperature to 550 °C annealing for 5 min, then cool down to 420 °C for the 2000 Å InAs buffer layer growth. During this growth, the substrate temperature is linearly ramped to 520 °C at a ramp rate of 8 °C/min.

Sample C: Ramp substrate temperature to 550 °C annealing for 5 min, then cool down to 420 °C for the 2000 Å InAs buffer layer growth. During this growth, the substrate temperature is set as linearly ramped to 505 °C at a ramp rate of 8 °C/min.

The Nomarski images of those three wafers after the growth are presented in figure 4.1. Specifically, the magnification of the eyepiece lens is 10x, and the objective lens used in this project are primarily 5x and 40x magnification. The morphology of Sample C is comparable with Sample B and the defect density of those two grows are significantly lower than Sample A, which indicates the growth condition of Sample B or C can be employed for the further growth.

Sample D is designed to include the 1.8 μm highly doped InAs bottom cladding layer, grown on the buffer layer deposited using parameters of growth C. The Nomarski images of 50x and 400x of the resulted morphology are shown in figure 4.2 (a) and (b). The plot of growth temperature measured by the manipulator thermocouple and ISP reading along with the In, As shutter opening status is shown in figure 4.2 (c).

The InAs growth rate for both buffer layer and 1.8 μm bottom cladding layer is set to 2.78 Å/s. The morphology of Sample D is comparable to the morphology of Sample C, which indicates that the very high Si doping (3×10^{19} cm^{-3}) does not influence much the growth kinetics.

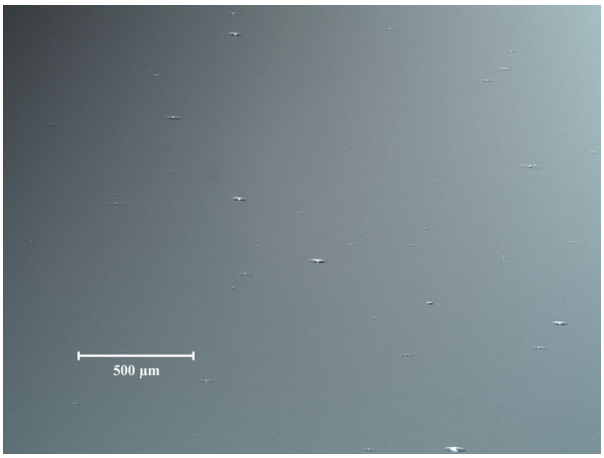

(a) ×50 magnification

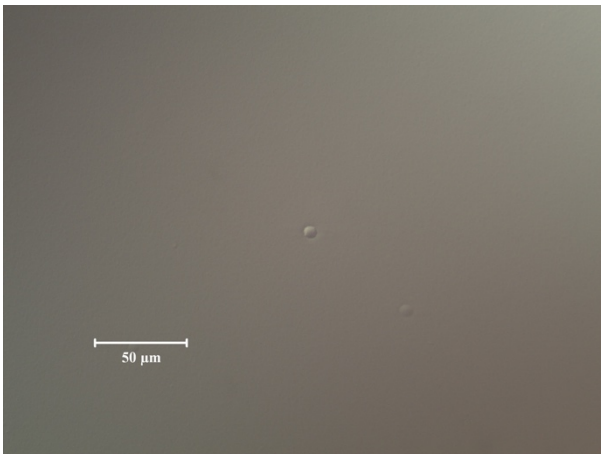

(b) ×400 magnification

(c)

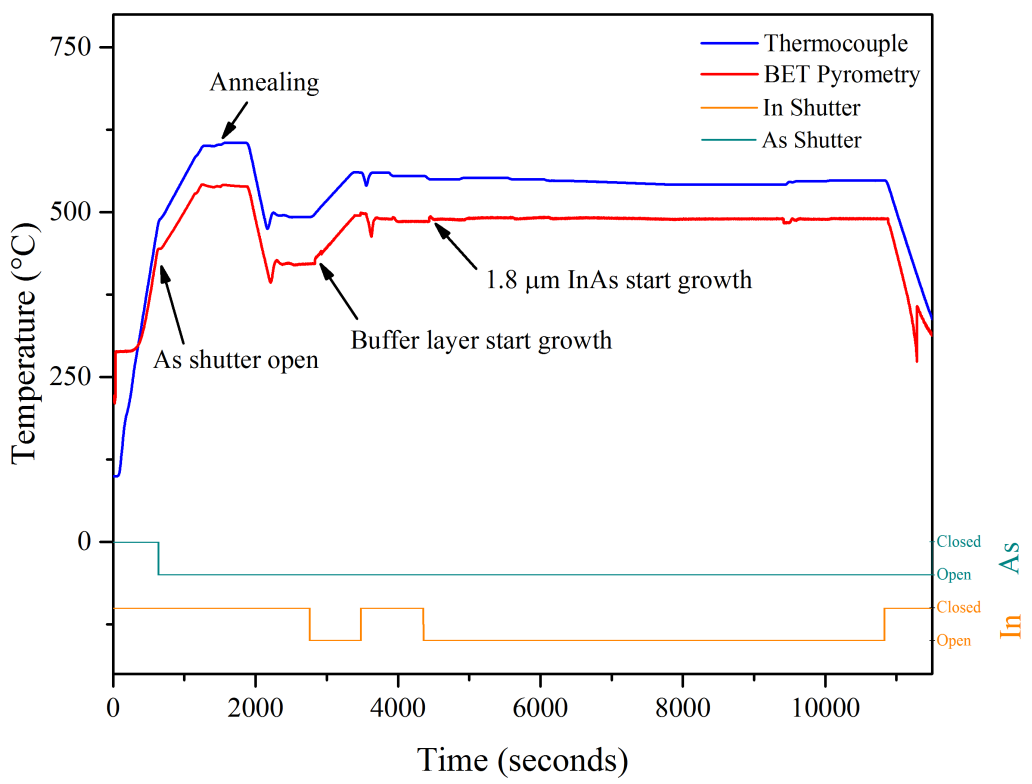

Figure 4.2: Nomarski images of Sample D (a), (b), and its growth condition plot (c).

4.1.2 Full structure growth

As a result of the ultra-thin film growth requirement of the QCL active region design, the top and bottom superlattice layer and the active region InAs and AlSb layers are grown with a growth rate of 1 Å/s. This required adjusting the In cell temperature to lower level corresponding to this InAs growth rate. The growth procedure used in Sample E will be introduced in this section.

Followed by the optimized growth conditions for buffer layer and bottom cladding layer, the next part of the structure, which consists of bottom 200 repeat (20 Å InAs / 20 Å AlSb) superlattice (SL) spacer, active region and another 200 repeats top SL spacer, was grown at 420 °C. After growing the top spacer, the In cell temperature was adjusted again to ensure 2.78 Å/s growth rate, and the top highly doped cladding layer was grown as the last element of the structure.

As discussed, the growth rate for buffer layer, 1.8 μm InAs bottom cladding layer and 1.5 μm InAs top cladding layer was 2.78 Å/s, while the growth rate for the rest of the layers was 1 Å/s. For that the In cell flux needed to be calibrated at two different temperatures corresponding to those two growth rates, and it required ramping between those temperatures during the real growth and also needed extra stabilization time. However, such cell temperature change processes could add an uncertainty of the growth rate for the critically important active region of the QCL. To circumvent this problem, another growth, Sample F, was performed with InAs growth rate of 1.5Å/s throughout the entire structure.

The Nomarski observation for Sample E are shown in figure 4.3 (a) and (b). The defect density is around 18.8 mm^{-2} in total, and 2.6 mm^{-2} if only take the defect size which is greater than 50 μm^{-2} into account. Most of the observed point defects are believed to be caused by InAs dust generated during cleaving, as well as contamination which is hard to avoid in this process. The shutter sequence for the bottom SL spacer growth along with the measured wafer temperature are plotted in figure 4.3 (c). The substrate temperature shows around 10 degree jumps at opening of Al and Sb shutters while starting AlSb growth, followed by more gradual increase by another 5 degrees, while on closing Al and Sb shutters the 10 degree jumps down

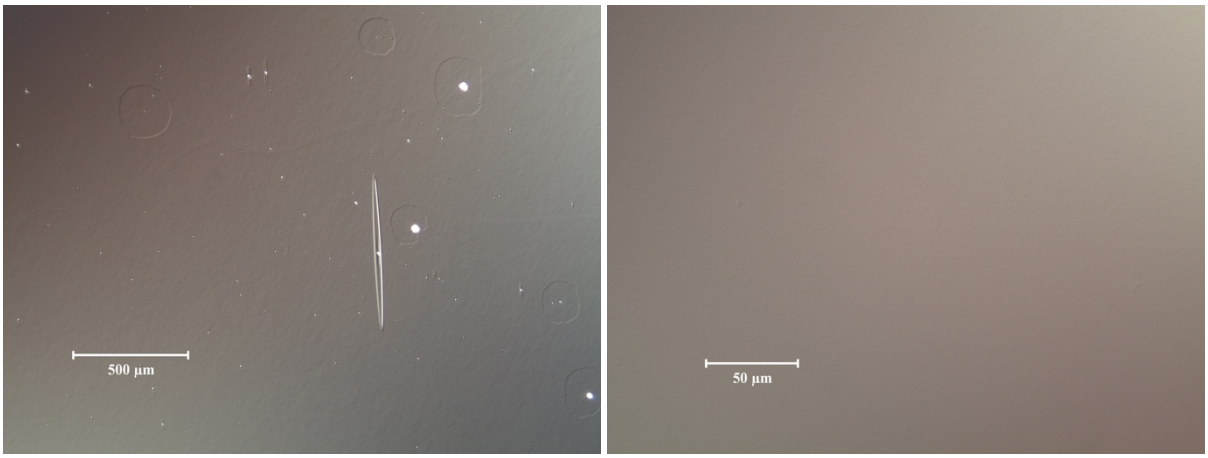

(a) ×50 magnification (b) ×400 magnification

(c)

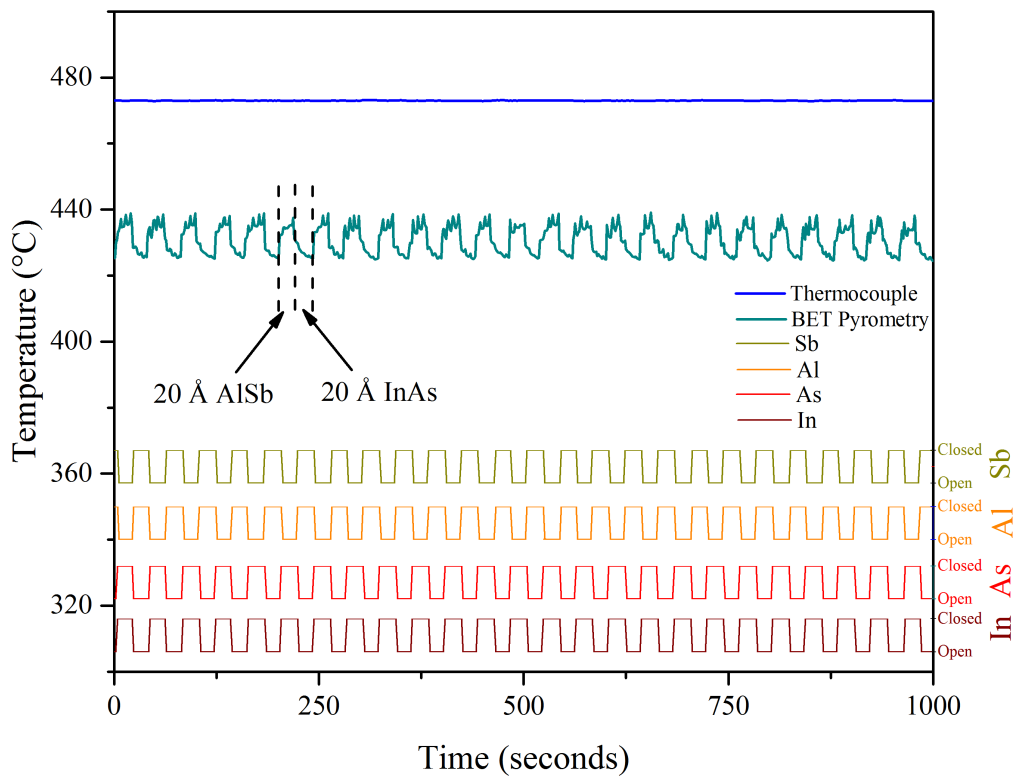

Figure 4.3: Nomarski images of Sample E (a), (b), and its growth condition plot (c).

happens first followed by 5 degree slow drift. The first effect (10 degree fast change) is an artifact of the ISP temperature measurement method, which picks up some of the scattered radiation from very hot Al and Sb cells, while the second, slow change is due to additional heating of the wafer by the radiation from these cells.

4.1.3 Processing and device characterization

Laser devices with disk mesa or ridge waveguide are fabricated out of Sample E. The SEM observations of the ridge waveguide device are shown in figure 4.4. The QCL devices are cleaved into laser bars with a cavity length of 1 mm. The laser ridge width ranges from 9 μm to 16 μm.

As shown in Figure 4.4(b), the cross-section SEM reveals clearly the bottom superlattice (SL) layer, the InAs/AlSb quantum well active region, the top SL layer and the top contact layer. There are some trenches observed near the edge of the side wall. These undercuts might be attributed to the anisotropic dry etch rate in the mesa etching step. The transition sections between two different regions, such as from 1.8 μm InAs layer to the 200 repeats AlSb/InAs SL regions or from top SL spacer to the 1.5 μm InAs capping layer, are weaker than the coherent growth regions with a certain repeat sequence or a single type material. The dry etch rate at those regions could be much faster, leading to the formation of the lateral undercuts. The fact that those trenches are only observed in the SL and active regions may provide indirect evidence to this hypothesis. Apparently, the reactive ion etch recipe needs to be further optimized to minimize the undercuts during mesa formation.

Figure 4.4 (c) shows part of the top surface of the fabricated ridge waveguide laser device under a low magnification. Some convex plate-shaped defects are observed near the edge of the sample. These defects were observed at the surface of as-grown wafer (Figure 4.3(a) and are still observable after the dry etch of the mesa structure (down to the 1.8 μm bottom cladding layer). This suggests the origin of the defects is located beneath the bottom SL spacer. Further optimization is still desired to eliminate those defects. The As overpressure might be playing an important role in the epi-layer growth optimization.

(a)

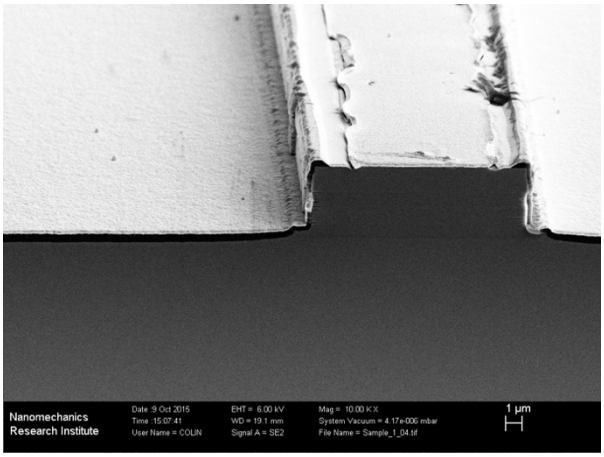

(b)

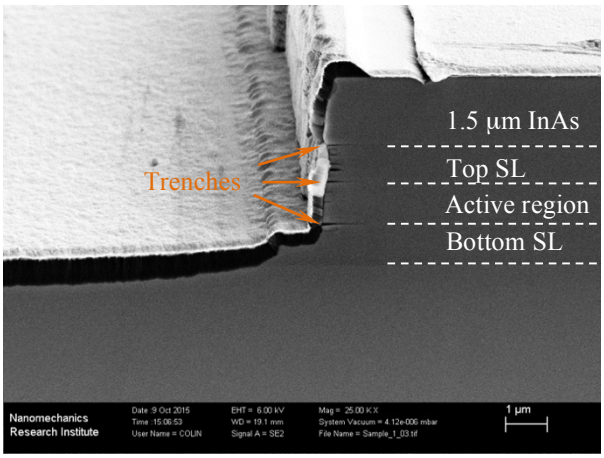

(c)

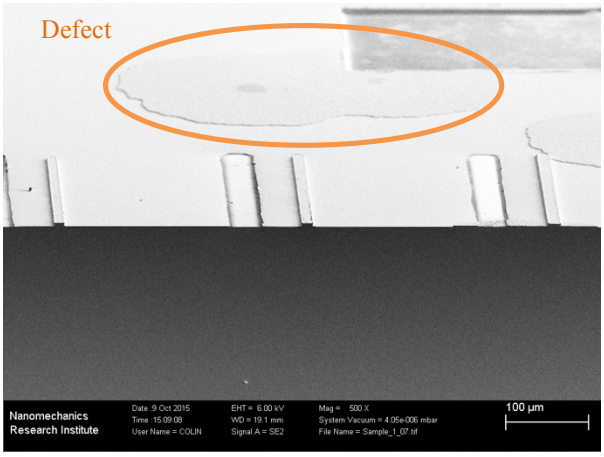

Figure 4.4: SEM observation of ridge waveguide MIR-QCL after processing under different magnification (a), (b) and (c).

The cleaved devices are mounted on a gold coated copper package via indium soldering. The reason for the using of copper as the package material is that oxygen-free copper shows excellent thermal conductivity which is around 10800 W/m•K at 20 K and 400 W/m•K at 300 K. The indium soldering is used to balance the thermal expansion difference between the copper and InAs substrate (1.5e-5 K^{-1} for Cu and 4.52e-6 K^{-1} for InAs).

The mounted devices are then wire-bonded with gold wires for electrical connection. Figure 4.5 (b) shows mesa-structure laser devices mounted on a LIV measurement setup. In terms of the LIV measurement, the device is biased by a pulse generator with a frequency of 1 kHz and a pulse width as 350 ns. The LIV result measured at 10 K is shown in figure 4.6 (a).

The threshold current density is measured to be 2.1 kA/cm^2. The measured lasing spectrum is shown in figure 4.6 (b). The spectrum exhibits lasing emissions at λ_1 = 3.4 μm and λ_2 = 3.44 μm in the working current range. Ridge-waveguide laser devices are still under optimization and will be tested once available.

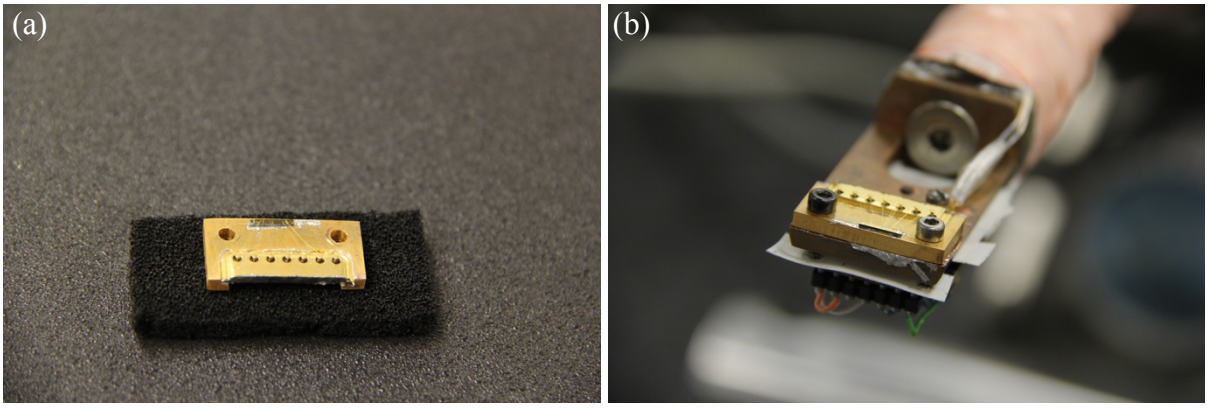

Figure 4.5: (a) General view of a MIR-QCL device, (b) device mounted on the LIV system.

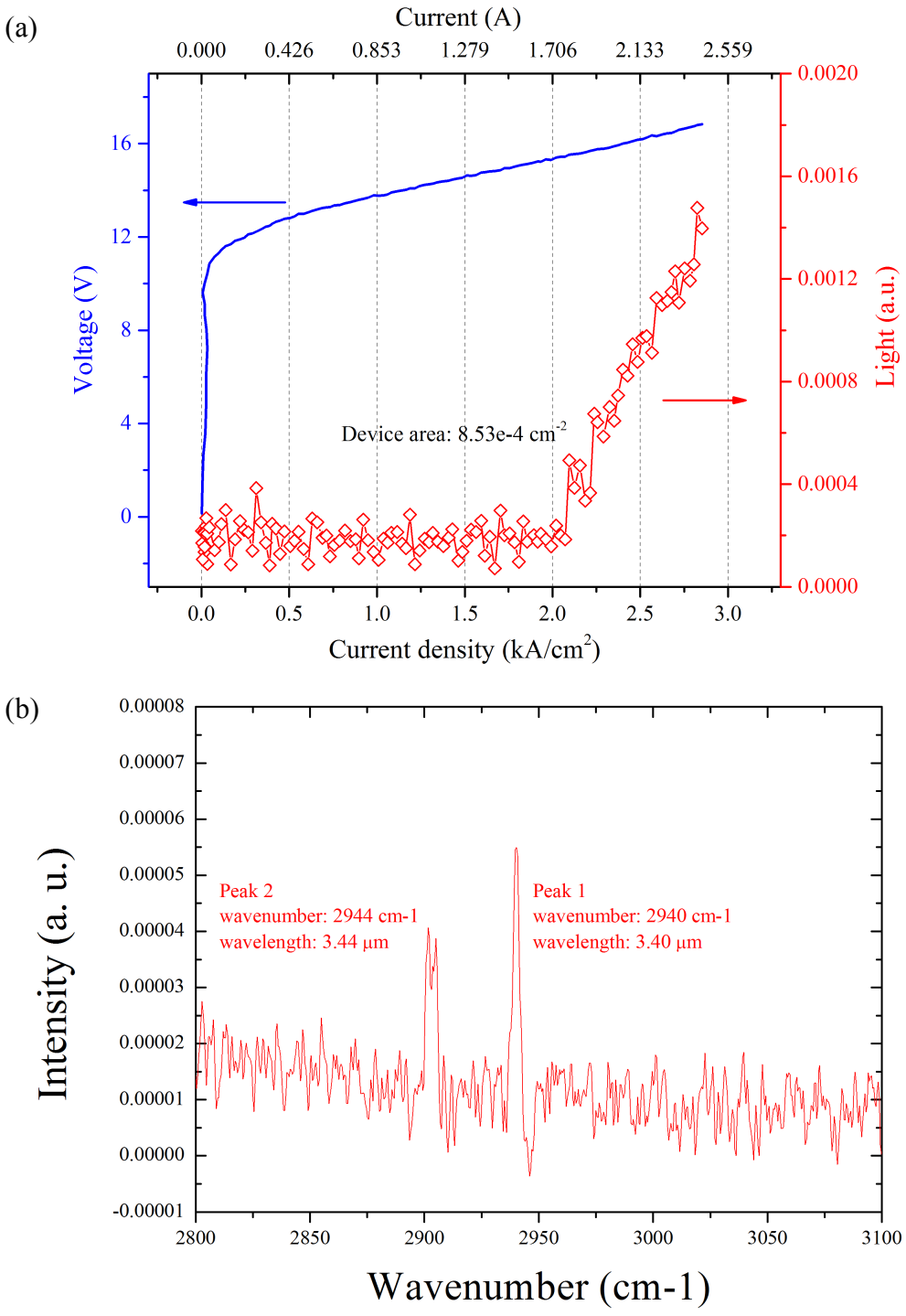

Figure 4.6: LIV (a) and FTIR (b) measurement of disk mesa waveguide device fabricated from Sample E.

4.2 XRD simulation

The XRD simulation is based on the Jordan Valley RADS software, version 5.2. Once the key parameters such as the substrate type and the sequence of layers, including their thickness and if needed compositions, are entered, the software calculates, using the dynamic X-ray diffraction theory, the expected ω-2θ scanning result which can be compared to the experiment. For a simple structure simulation, the software is able to do an automated fitting using a genetic fitting algorithm.

However, for a MIR QCL device, as a result of its complex structure resulting in a very complicated XRD ω-2θ scanning pattern, the automatic approach is not suitable. An alternative method is based on combining single-shot simulations with the simple algebra rooted in the understanding of the superlattice peaks positions and how they are influenced by the superlattice period and average strain in each period.

The fitting strategy used in this project is based on the second method. The process is divided into three main parts which are the SL spacers simulation, full structure simulation, and AlAs type interface simulation study.

4.2.1 SL cladding simulation

All the models are based on a set of standard settings. The X-ray wavelength used in this project is 1.54056 Å and the Bragg reflection geometry is (004). The simulation range is set from -7500 sec to 7500 sec with step size of 4 sec, the same as the experimental scanning settings.

The SL spacer model is shown in figure 4.7. It consists of a 200 repeats of InAs/AlSb layers of the bottom SL spacer, a 11834.5 Å equivalent active region (AR) layer, another 200 repeats of InAs/AlSb of the top SL spacer and a 1.5 μm InAs cap layer. In order to subtract the complex active region superlattice peaks and highlight the SL spacer peaks, the AR layer is simplified as an alloy layer $In_xAl_{1-x}As_ySb_{1-y}$ with the thickness set to the sum of all the active region layer thickness. The fraction x and y are calculated as 0.662 which is approximately the ratio of the total thickness of InAs in the active region to the thickness of this region.

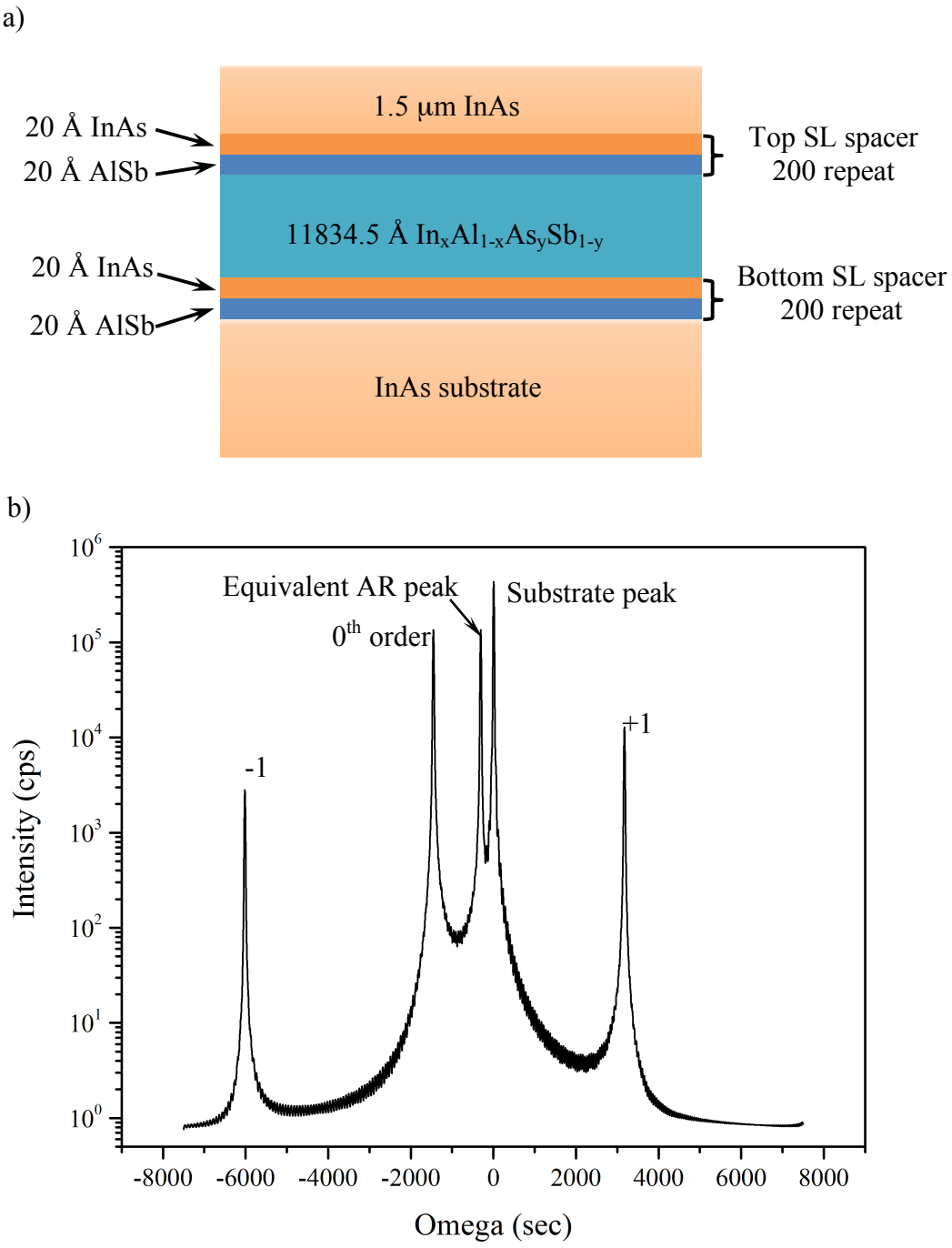

Figure 4.7: (a) Schematic view of the modeled structure. (b) XRD simulation result of the structure shown in (a).

The first attempt is designed to find the relationship between the angular separation from -1 to +1 satellite peaks and the SL thickness with a fixed AlSb/InAs ratio of 1:1. The detailed model parameters is listed in table 4.1.

With the fixed AlSb/InAs ratio, the angular separation between the -1th order and +1th order peaks is decreased as the SL thickness increasing, but the zero-order peak position is stable without any change. The XRD simulation patterns based on those models are plotted in figure 4.8 (a), and the reciprocal of ±1 satellites spacing corresponding to different SL thickness is shown in figure 4.8 (b). The reciprocal of satellites spacing is linearly related to the SL thickness. In other words, the satellites spacing is inversely proportional to the SL period. It satisfies the equation $D = \frac{(p-q)\lambda}{\Delta\theta_{p,q} cos\theta_B}$, derived in Chapter 2, where D is the angular separation between SL peaks.

The second step is designed to find the relationship between a single period structure (i.e. proportion between InAs and AlSb layer thicknesses) and the related SL peaks shift. The SL period thickness is fixed at 40 Å and the repeat is set as 200. AlSb layer thickness is varied from 14 Å to 26 Å with a step size of 2 Å. The simulation result is shown in figure 4.9. Both

Table 4.1: Estimated -1th, 0th, +1th order peak position with different SL thickness.

SL thickness	-1th order		0th order		+1th order		1/Angle (1/sec)
	Omega(sec)	Intensity	Omega(sec)	Intensity	Omega(sec)	Intensity	
34 Å	-6816	1345.241	-1452	1.52722E7	3996	8481.1533	9.249E-5
36 Å	-6520	1754.8286	-1452	1.52722E7	3692	9862.3428	9.792E-5
38 Å	-6256	2235.6416	-1452	1.52722E7	3420	11226.216	1.033E-4
40 Å	-6016	2793.5542	-1452	1.52722E7	3172	12831.06	1.088E-4
42 Å	-5800	3440.3088	-1452	1.52722E7	2952	14666.989	1.143E-4
44 Å	-5604	4170.2158	-1452	1.52722E7	2752	16053.905	1.197E-4
46 Å	-5424	4941.7178	-1452	1.52722E7	2568	18409.92	1.251E-4

of the 0^{th} order and satellite peaks are shifting, however, the SL satellites spacing remains fixed, as expected from the fixed period of the SL.

This means the Al content of each SL repeat, which is responsible for the average strain of the SL with respect to InAs lattice constant, affects the entire XRD pattern, shifting all peaks at the same time without changing their relative angular separation.

Based on those two steps, we can conclude that the average SL layer thickness can be calculated as long as the corresponding satellite peaks, used to determine the satellites spacing, are positively identified in the experimental diffractogram. The full MIR QCL structure contains three different superlattices: the bottom SL spacer, the active region SL and top SL spacer. In principle to top and bottom SL spacers should have the same period and strain, giving SL reflections peaks in the same positions. However, even a small drift of the fluxes used over the time between the growth of the bottom and top SL spacer, can displace these peaks from each other. Thus in general the XRD pattern may consist of three different sets of satellite peaks. It is very important to properly identify them in the diffractogram. The strategy used in this project can be divided into four steps.

Step 1: find the top SL -1 and +1 satellite peaks and calculate the top SL average layer thickness. Generally, the top SL -1 satellite peak is located between -5000 sec and -4000 sec, and the +1 satellite peak is generally located from 4000 sec to 5000 sec in a real MIR-QCL structure diffractogram. It is slightly different than the satellites position shown in figure 4.8 (a) and figure 4.9. Those additional shifts result from predominantly AlAs-like interfaces in a real growth structure and it will be discussed in more details in step 4. However, since the first three steps are focused on the SL average layer thickness fitting, a phenomenological strain values are employed within the models for the first three steps, without explicitly considering interfacial strain. An important feature helping to distinguish the bottom SL from the top SL satellites is based on the satellites intensity. Since the bottom SL is much deeper under the surface, the intensities of its satellite peaks are significantly lower than the top SL spacer. However, those lower intensity peaks are easily mixed up with the active region satellites which can be comparable in intensity at these angular locations.

a)

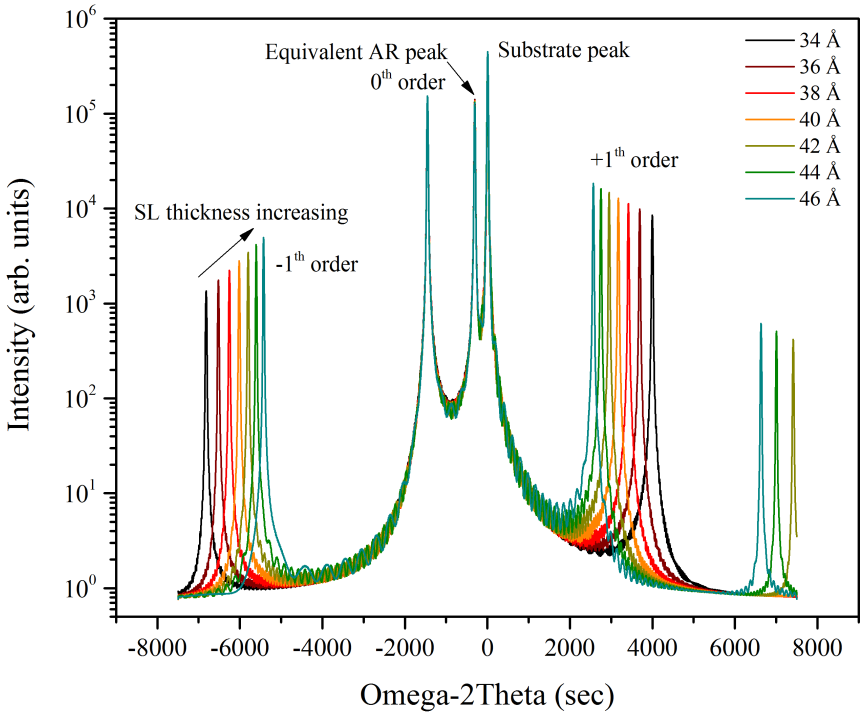

b)

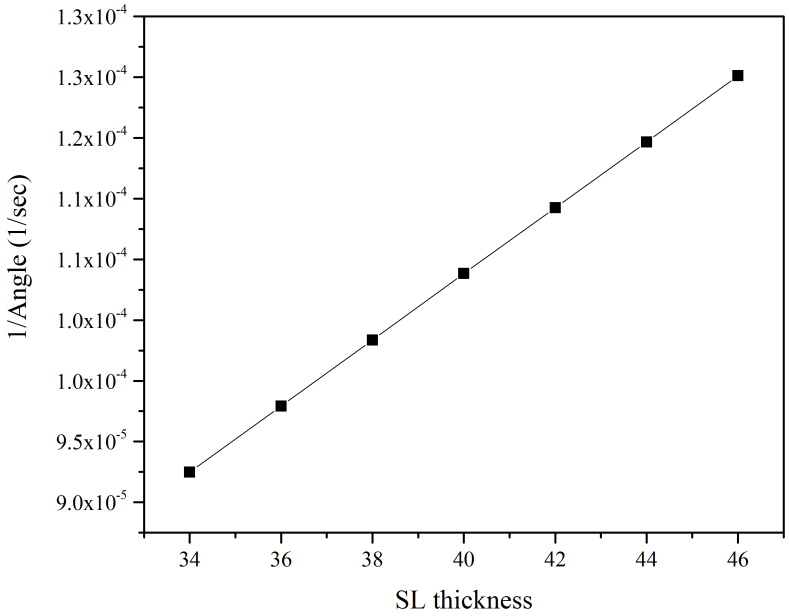

Figure 4.8: (a) Simulation XRD patterns for different SL thickness with a fixed InAs to AlSb ratio. (b) Plot of the reciprocal of the angular separation with various SL thickness.

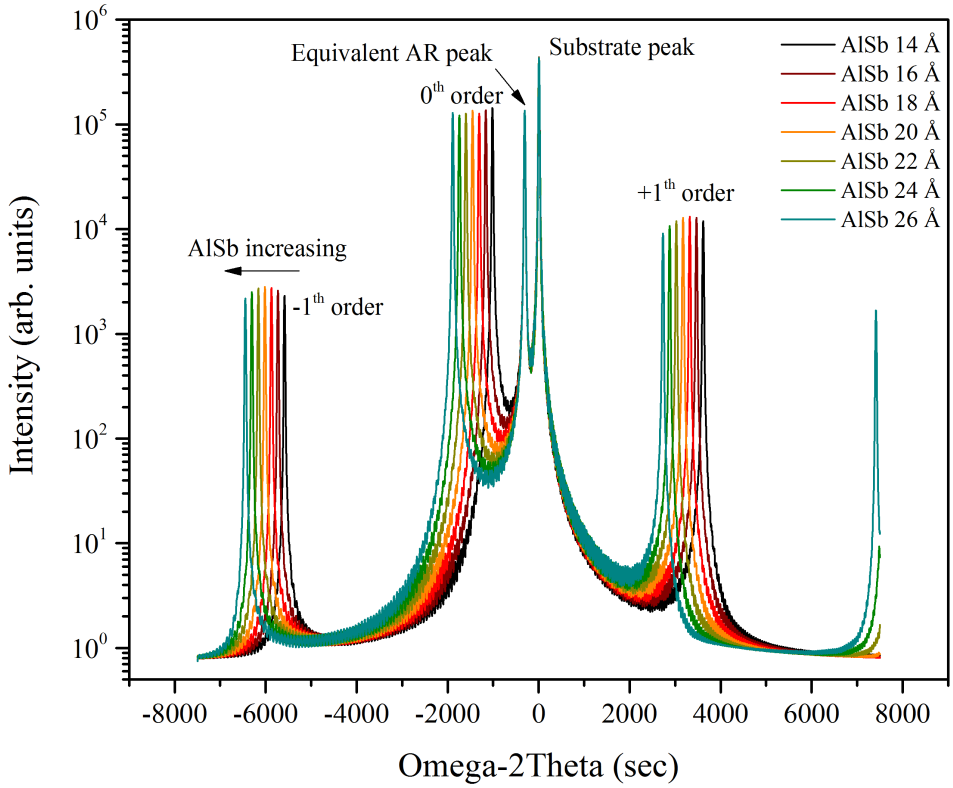

Figure 4.9: Simulation XRD patterns for different AlSb layer thickness within a fixed SL thickness of 40 Å.

Here, we just make a temporary assumption that the bottom SL reflections overlap with the top SL. Once the top SL and active region peaks are identified, then subtracted from the experimental pattern, the remaining peaks can be identified as related to the bottom SL. Figure 4.10 shows the top SL fitting result of Sample F at the end of step 1. Extracted from the experimental pattern, the $+1^{th}$ and -1^{th} satellite are located at 4368 sec and -4624 sec, respectively, giving the separation of 8992 sec, thus the average period thickness of top SL, based on the fitting in figure 4.8b, is calculated as 41.03 Å, that is 2.58 % thicker than the targeted value of 40 Å.

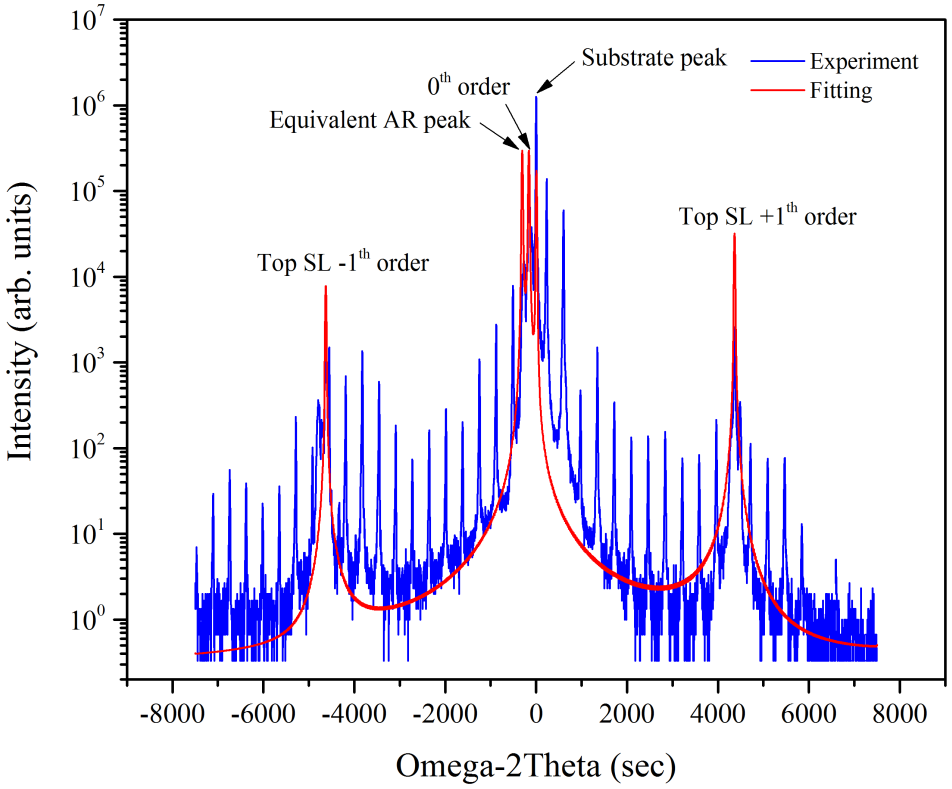

Figure 4.10: Plot of Sample F XRD scanning with top SL fitting curve.

4.2.2 Full structure simulation

The full structure simulation mainly focused on extracting the thickness of the individual period of the active region and spacer SLs, as well as the net strains for these layers. Together with the atomic flux measurements done before and after the QCL growth, such simulations allow to estimate accurately the thickness of all the individual layers.

Step 2: based on the satellites spacing, calculate the thickness of the active region period. All the significant peaks in the diffractogram are identified and marked using a matlab code listed in Appendix A (figure 4.11), while their positions and intensities are listed in table 4.2. AR and SL represent active region peaks and superlattice peaks, respectively. Some of the peaks are marked as N/A which means those peaks cannot be identified at this step.

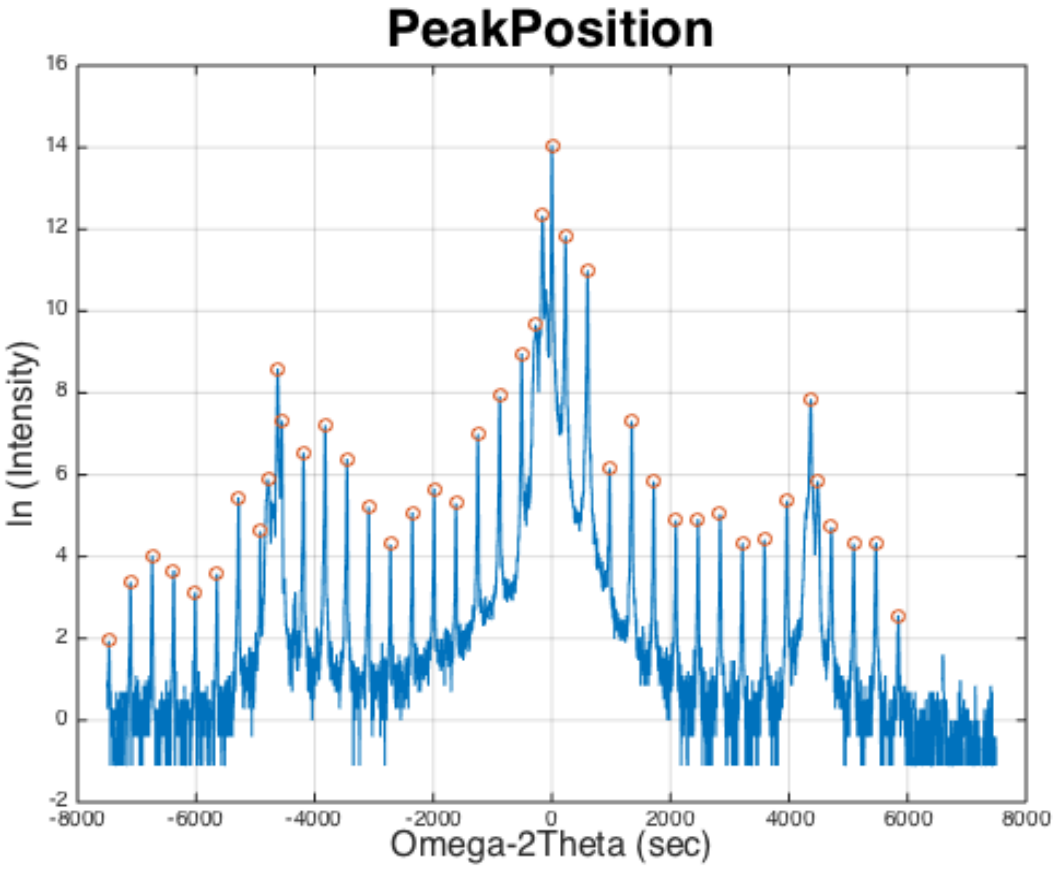

Figure 4.11: Peak finder used to identify the peak position.

Table 4.2: Peak position data extracted from XRD result of Sample F

Peak ID	Position (sec)	Intensity	Neighbouring peak separation	Comment
1	-7472	6.99	368	AR
2	-7104	29.30	364	AR
3	6740	55.96	360	AR
4	-6380	38.92	360	AR
5	-6020	22.65	372	AR
6	-5648	35.95	360	AR
7	-5288	232.31	372	AR

8	-4916	102.22	124	AR
9	-4792	364.14	168	Bottom SL
10	-4624	5402.76	72	Top SL
11	-4552	1504.46	364	AR
12	-4188	693.66	364	AR
13	-3824	1353.24	368	AR
14	-3456	597.72	364	AR
15	-3092	184.87	368	AR
16	-2724	73.91	372	AR
17	-2352	160.87	368	AR
18	-1984	287.02	368	AR
19	-1616	200.73	368	AR
20	-1248	1090.81	368	AR
21	-880	2763.77	372	AR
22	-508	7824.87	236	N/A
23	-272	15837.15	112	AR
24	-160	227626.08	160	N/A
25	0	1259919.50	232	Substrate
26	232	138159.67	372	AR
27	604	59705.81	368	AR
28	972	473.23	372	AR
29	1344	1500.99	376	AR
30	1720	342.85	372	AR
31	2092	133.80	372	AR
32	2464	137.53	372	AR
33	2836	154.56	380	AR
34	3216	76.24	368	AR
35	3584	82.91	380	AR
36	3964	213.48	404	AR
37	4368	2568.18	116	Top SL
38	4484	347.85	232	Bottom SL
39	4716	112.51	376	AR
40	5092	75.62	380	AR
41	5472	76.90	368	AR
42	5840	12.98		AR

The scanning step size is set as 4 sec. The angular separation between each two neighbouring peaks is calculated as shown in table 4.2. After removing the identified in step1 peaks related to SL spacers, most of the remaining peaks are spaced within the range from 368-372 sec from each nearest neighbour, with average value of 369.55 sec. In the example discussed, the average thickness of active region period calculated based on this value is 3.27 % larger than the target. Applying this correction factor to the active region layer thicknesses, one obtains the simulated diffractogram result as shown in figure 4.12. As discussed in previous section, the bottom SL satellite peaks are much weaker and generally located very close to the top SL ones, or overlap them if the fluxes stability was sufficiently good thought the growth. Comparing the updated fitting curve with experimental result, two peaks close to the top SL -

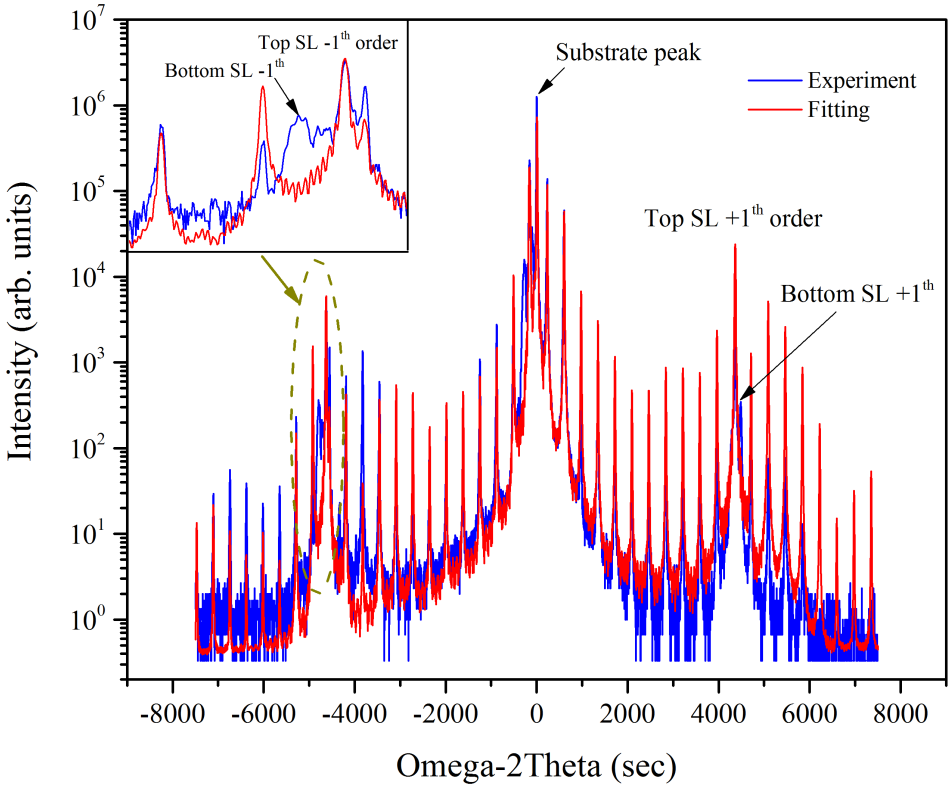

Figure 4.12: Plot of Sample F XRD scanning with active region fitting curve

1 and +1 satellites, respectively are identified as belonging to the bottom SL spacer. One of them is shown in the zoomed-in inset of figure 4.12.

Step 3: Based on the angular separation of the identified above bottom SL spacer satellites, the period thickness of the bottom SL can be calculated, using the same strategy as for the top SL calculation. The -1 and +1 satellites of this sample are measured as -4792 sec and 4484 sec, respectively, which gives the angular separation of 9276 sec. Inserting this value into the linear dependence extracted from figure 4.8 (b), gives the average layer thickness of bottom SL spacer of 39.78 Å which is 0.56 % less than the target value. Inserting these values into the QCL structure and running the RADS simulation produces result shown in figure 4.13, which account now for all the peaks location.

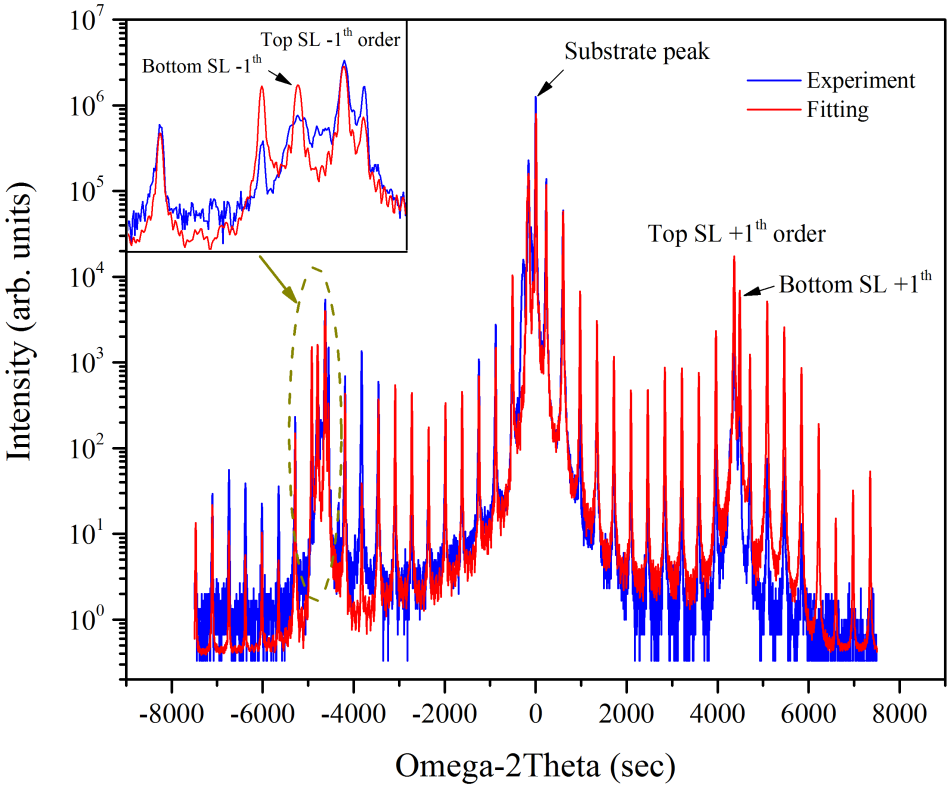

Figure 4.13: Plot of Sample F XRD scanning with active region and bottom SL fitting curve

The first three steps are focused on deriving the thicknesses of the periods for the three stacks, the two SL spacers and the active region. Each of these periodic stacks is responsible for a set of equally spaced diffraction peak, and the spacing between these peaks can be measured very accurately. However, the position of each peak set with respect to the Bragg reflection from the InAs substrate is very sensitive to the average vertical strain in each period. To align the simulation peaks with their experimental position (as shown in Fig 4.12 and 4.13) the average strain for each AlSb layer was entered manually. This is equivalent to assuming that instead of AlSb all barriers are made of $AlAs_xSb_{1-x}$ with x fraction which may be different for each of the stacks. Indeed, such average strain will depend on the excess arsenic in each

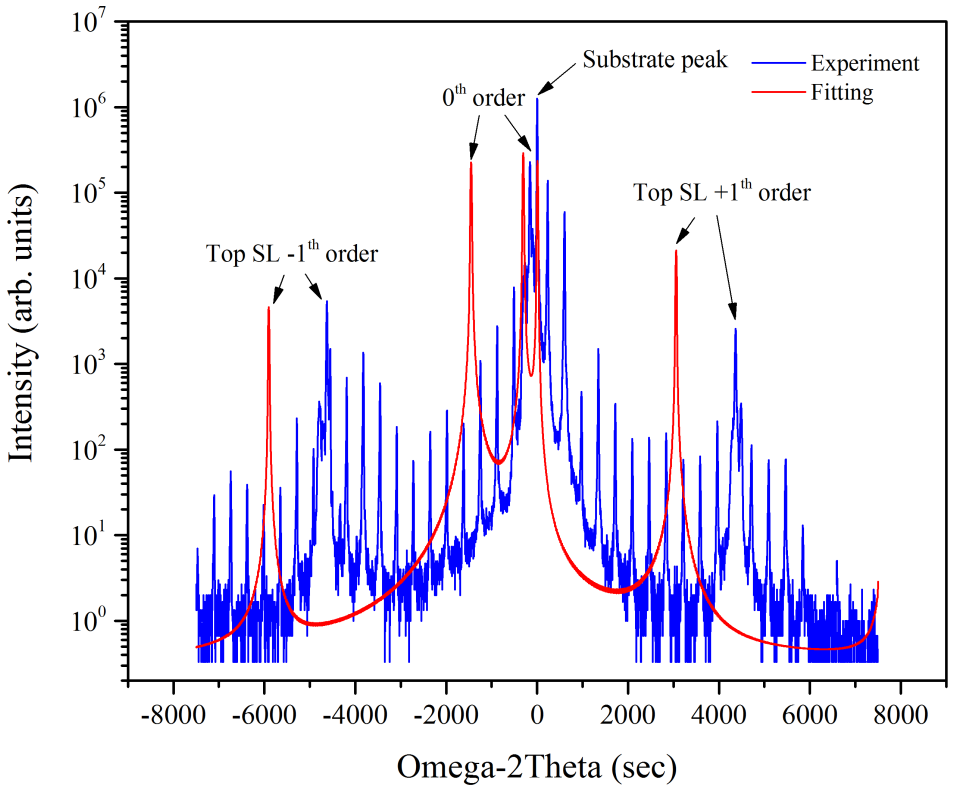

Figure 4.14: Plot of Sample F XRD scanning with a pure InAs/AlSb SL fitting.

period, compared to a situation where pure InAs and AlSb layers are grown and the interfaces between them are of unstrained mixed AlAs/InSb type. However, the relative intensities of the superlattice satellite reflections are governed by the exact distribution of the excess arsenic in AlSb, as well as possible segregation effects which may involve In or Sb migration across the interface in the growth direction. This will be discussed in the following section.

4.2.3 Interface simulation

Step 4: Interface related XRD simulation. As a result of the active region consisting of tens of InAs/AlSb sequences with different layer thicknesses in a single repeat unit, which makes the interface formation much more complicated, the simulations of the interface strain are based

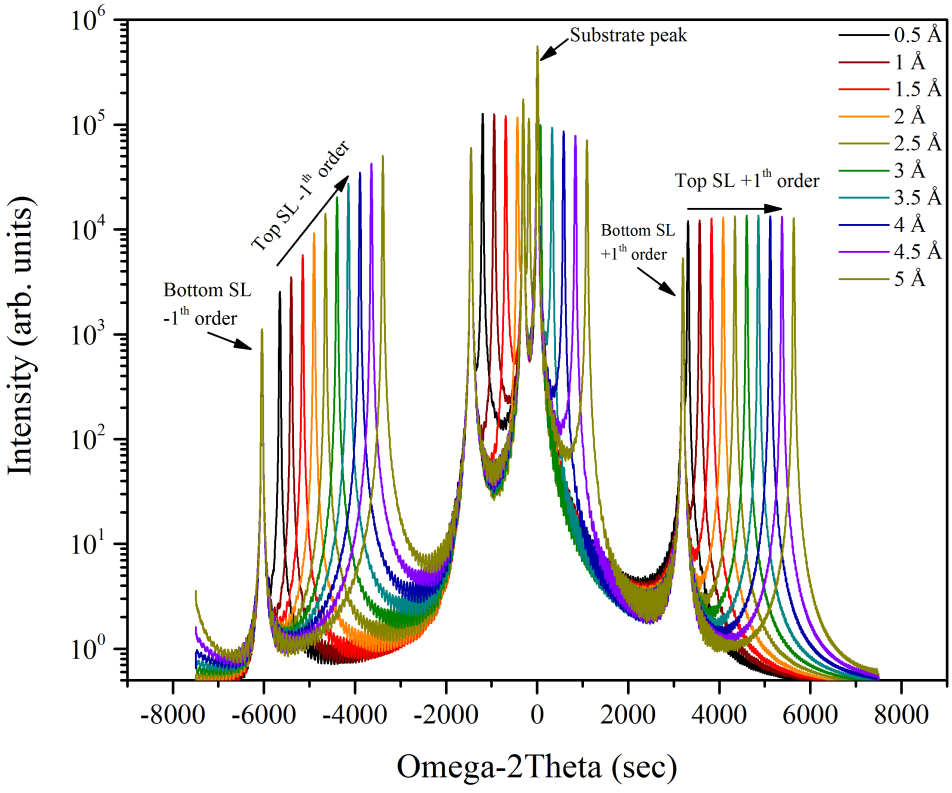

Figure 4.15: Simulation XRD patterns for different AlAs layer thickness within InAs/AlSb SL.

(a)

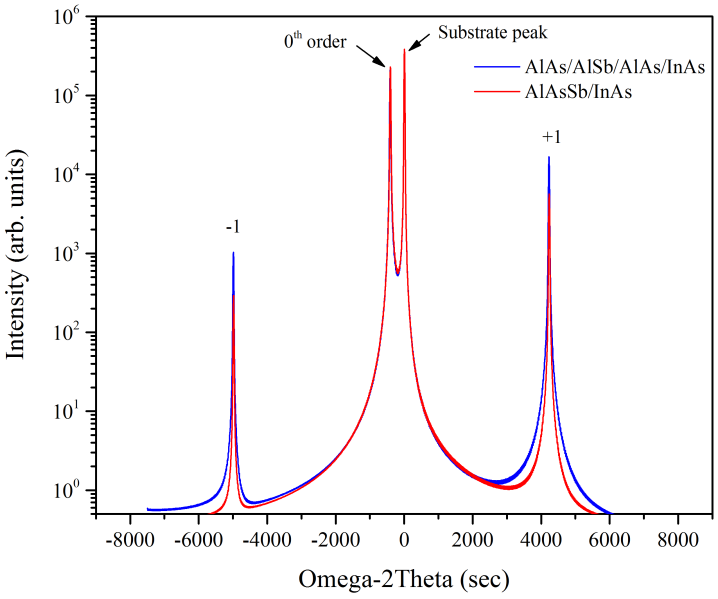

(b)

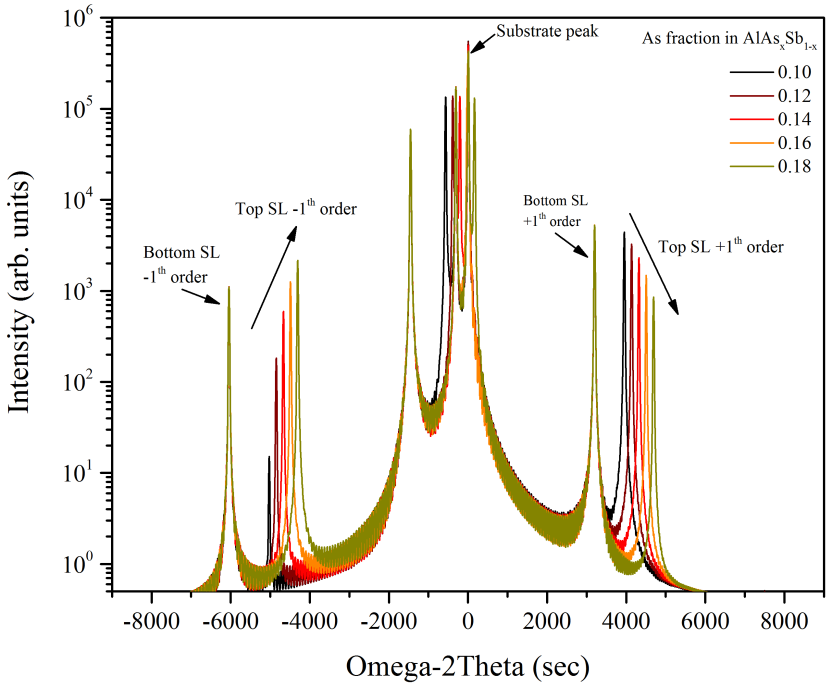

Figure 4.16: (a) XRD simulation of AlAs/AlSb/AlAs/InAs (1/18/1/20 Å), and 20 Å AlAsSb / 20 Å InAs, (b) Plot of different As fraction in $AlAs_xSb_{1-x}$ with fixed layer thickness of InAs and $AlAs_xSb_{1-x}$.

on the top SL of Sample F in this section. The simulated XRD curve of the structure, which consists of a pure 20.52 Å InAs / 20.52 Å AlSb SL, is shown in figure 4.14. The experimental curve is shifted towards the higher angles, which indicates presence of additional tensile strain within the SL stack. As calculated in section 2.2.2, the vertical lattice constant of AlAs grown on InAs is 5.279 Å, which is smaller by more than 17 % than AlSb layer it replaces. Hence, by adding the AlAs between InAs/AlSb, the fitting curve tends to shift to higher angles (figure 4.15), corresponding to smaller average vertical lattice constant. A total extra thickness of 2.55 Å AlAs needs to replace AlSb at the interface to explain the observed shift of the superlattice reflections for the SL spacer. This corresponds to 0.97 ML of fully strained AlAs on InAs. More likely, a predominantly AlAs-interfaces are present at both InAs/AlSb and AlSb/InAs interfaces.

However, the same shift could also be obtained by a certain percent of As in AlAsSb (instead of AlSb), as shown in figure 4.16 (a). The XRD simulation shows the diffractogram from AlAs/AlSb/ AlAs/InAs (1/18/1/20 Å) which overlaps the $AlAs_{0.12}Sb_{0.88}$/InAs (20/20 Å) structure diffractogram, except for the satellite peaks intensity. The plot of SL with the equal layer thickness of 20.52 Å InAs and $AlAs_xSb_{1-x}$ with different x fraction is shown in figure 4.16 (b). Compared with the experiment curve, the As fraction is determined as 0.14, which means an equivalent layer $AlAs_{0.14}Sb_{0.86}$ would matched the experiment data. In reality we most likely have different percent of AlAs ML at each interface and some As in AlSb layer. The latter is most likely not uniformly distributed, since background As left after growing InAs is exponentially decaying in the chamber as we grow AlSb. The complications which would result from a more complex atom mixing at the interfaces, that is possible In segregation from InAs into AlSb and Sb segregation from AlSb into InAs, require more detailed investigation which goes beyond the scope of this thesis.

Chapter 5

Conclusion and Future Work

This thesis presents a work on InAs/AlSb based mid-IR QCLs growth condition optimization, effective modeling for HRXRD full structure diffractogram fitting and interface study based on the XRD ω-2θ scanning curve simulation. The major accomplishments and experimental observations, achieved in this project, are listed below:

- Reliable InAs substrate temperature monitoring is realized in this project for the first time. As designed, the MIR-QCL is grown on a n-doped InAs (100) substrate. Instead of detecting the position of the absorption edge from the transmission spectrum, which is generally used by conventional BET measurement, the substrate temperature is determined by integration over the spectral range from 900 to 1700 nm of the light intensity emitted by InAs wafer.
- The growth condition of the MIR-QCL is optimized to obtain atomically smooth surface morphology and structurally perfect crystalline layer with strain entirely accommodated by elastic distortion rather than dislocation generation.

- Some convex plate-shaped defects are observed at the surface of as-grown wafer and are still observable after the dry etch of the mesa structure, which indicates the origin of the defects is located beneath the bottom SL spacer. It suggests that the further optimization is still desired to eliminate those defects.
- The MIR-QCL devices with disk mesa or ridge waveguide are fabricated, respectively. The disk-loaded waveguide device is demonstrated lasing at 3.4 μm with a threshold current density of around 2.1 kA/cm^2 at cryogenic temperature. Ridge-waveguide laser devices are still under optimization and will be tested once available.
- A full structure InAs/AlSb based QCL XRD modeling is designed to calculate the individual SL region average layer thickness. The fitting is based on a ω-2θ scanning curve. Bottom SL, active region and top SL average layer thickness can be extracted. In a most recent growth sample, the deviation from target parameters for those three regions are only 1.08 %, 0.82 % and 0.69 %, respectively, which shows the highly controllable growth rate over the long period growth.
- The RADS simulation indicates displacement of some of Sb by As. The exact location of AlAs bonds is not clear, but if located entirely at InAs/AlSb interface it would be equivalent to of 2.55 Å AlAs (slightly less than 1ML) in Sample F. Alternatively, if evenly distributed across AlSb barrier it would result in a superlattice with x fraction of 0.145 in $InAs_xSb_{1-x}$/InAs structure, instead of AlSb/InAs superlattice. However, in reality, the percent of AlAs at each interface and some As in AlSb layer is expected given the specific growth conditions.

Further investigations can be made as followed:

- As a result of the material switching during the active region or SL spacer growth, the temperature monitored by the ISP shows deviation reaches to 15 degrees. The compensation value is not suitable to keep switching within such a short period (typically several seconds). An algorithm presented by Johnson *et al*. is used to correct the apparent temperature errors, which is mainly result from the interference

and absorption during the epi-layer growth [49]. They determine the temperature based on the knee region position of the transmission spectrum measured by BET, and the width of the spectrum referring to the sharpness or curvature of the bend in the spectrum at the knee. As a result, the temperature oscillation is reduced to ±3 °C. This algorithm is desired to be tested during the MBE growth.

- The point defect density is still fairly high. Since the surface morphology in-between the defects is excellent we attribute most of these defects to substrate contamination during the cleaving of the substrates. Growth on full 2" InAs substrates should elucidate that issues.
- It is clear that some displacement of Sb by As is happening in the structure. This is desirable, since it effectively lowers the strain and prevents inelastic relaxation though dislocation generation, which would degrade the laser performance. However, the proposed modeling is not able to pinpoint the strain distribution within each period. Also the model has not been applied to the active region of the QCL. Future modeling should include the active region, as well as utilize the information embedded in the distribution of peak intensities of active region superlattice reflection which is influenced by the inner structure of each period.

Appendix A

MATLAB Peak Finder

```
%This script is used for the peak finding based on the HRXRD %data.

format long
load SampleF.mat;
plot(A,log(B),'-');
% axes('FontSize',16);
xlabel('Omega-2Theta (sec)','FontSize',16);
ylabel('ln (Intensity)','FontSize',16);
grid on;
hold on;
bc=[];
%bc is the boundary condition for the peak fitting
t=peakFind(A,B,9,1,[-7500,7500,1,inf],bc);
t(all(t==0,2),:)=[];

plot(t(:,1),log(t(:,2)),'o');
title('\fontsize{24}PeakPosition');
hold off;

function peak=peakFind(x,y,s,opt,Range,bc)
%s: peak check range (-s, s)
```

```
%opt: average condition, compared with the average peak intensity
within (-s,s)
[rx,cx]=size(x);
[ry,cy]=size(y);
if  rx==1
    x=x';
    rx=length(x);
end
if  ry==1;
    y=y';
    ry=length(y);
end
if  rx~=ry
    fprintf('%s','Vector element must agree!');
    return
end

numP=1;
numP2=1;
Data=sortrows([x,y]);
peak_initial = zeros (1000,2);
for i=1:rx
  isP=getPeak(Data,i,s,opt);
    if  sum(isnan(isP))==0

        peak_initial(numP,:)=isP;

        isP2=peakFilter(isP,bc);
            if sum(isnan(isP2))==0
                 peak(numP2,:)=isP2;
                 numP2=numP2+1;
            end
```

```
        numP=numP+1;
    end

end

function peak2=peakFilter(data,bc)
x=data(1);
y=data(2);
a= bc(:,1)';
b=max (a(a<x));
c=find (a==b);

intensity=(log(bc(c+1,2))-log(bc(c,2)))/(bc(c+1,1)-bc(c,1))*(x-
bc(c+1,1))+log(bc(c+1,2));

    if log(y)>=intensity,
                peak2=[x y];
            else
                peak2=[nan,nan];
    end
end

function p=getPeak(Data,i,s,opt)
%function p=getPeak(Data,i,s,opt,precord)
if i-s<1
    top=1;
else
    top=i-s;
end
y=Data(:,2);
if i+s>length(y)
    bottom=length(y);
else
```

```
    bottom=i+s;
end

tP=(sum(y(top:bottom)>=y(i))==1);
a=y(i)/mean(y(top:bottom));
if tP==1 && a>opt
    p=Data(i,:);
else
    p=[nan,nan];
end
```

References

[1] Faist, J., Capasso, F., Sivco, D. L., Sirtori, C., Hutchinson, A. L., & Cho, A. Y. (1994). Quantum Cascade Laser. *Science*, 264(5158), 553-556. doi:10.1126/science.264.5158.-553.

[2] Faist, J., Gmachl, C., Capasso, F., Sirtori, C., Sivco, D. L., Baillargeon, J. N., & Cho, A. Y. (1997). Distributed feedback quantum cascade lasers. *Applied Physics Letters*, 70(20), 2670-2672. doi:http://dx.doi.org/10.1063/1.119208.

[3] Beck, M., Hofstetter, D., Aellen, T., Faist, J., Oesterle, U., Ilegems, M., . . . Melchior, H. (2002). Continuous Wave Operation of a Mid-Infrared Semiconductor Laser at Room Temperature. *Science*, 295(5553), 301-305. doi:10.1126/science.1066408.

[4] Tredicucci, A., Gmachl, C., Capasso, F., Sivco, D. L., Hutchinson, A. L., & Cho, A. Y. (1998). A multiwavelength semiconductor laser. *Nature*, 396(6709), 350-353.

[5] Gmachl, C., Sivco, D. L., Colombelli, R., Capasso, F., & Cho, A. Y. (2002). Ultra-broadband semiconductor laser. *Nature*, 415(6874), 883-887.

[6] Devenson, J., Teissier, R., Cathabard, O., & Baranov, A. N. (2008). InAs-based quantum-cascade lasers. *Proc.SPIE*, 6909, 69090U1-69090U9. doi:10.1117/12.767653.

[7] Semtsiv, M. P., Wienold, M., Dressler, S., & Masselink, W. T. (2007). Short-wavelength ($\lambda \approx 3.05\mu m$) InP-based strain-compensated quantum-cascade laser. *Applied Physics Letters*, 90(5), 051111. doi:http://dx.doi.org/10.1063/1.2437108.

[8] Revin, D. G., Cockburn, J. W., Steer, M. J., Airey, R. J., Hopkinson, M., Krysa, A. B., . .

. Menzel, S. (2007). InGaAs⁄AlAsSb⁄InP quantum cascade lasers operating at wavelengths close to 3μm. *Applied Physics Letters*, 90(2), 021108. doi:http://dx.doi.org/10.1063/-1.2431035.

[9] Devenson, J., Teissier, R., Cathabard, O., & Baranov, A. N. (2007). InAs/AlSb quantum cascade lasers emitting below 3 μm. *Applied physics letters*, 90(11), 1118.

[10] Baranov, A. N., & Teissier, R. (2015). Quantum cascade lasers in the InAs/AlSb material system. *IEEE Journal of Selected Topics in Quantum Electronics*, 21(6), 85-96.

[11] Nicolai, J., Gatel, C., Warot-Fonrose, B., Teissier, R., Baranov, A. N., Magen, C., & Ponchet, A. (2014). Elastic strains at interfaces in InAs/AlSb multilayer structures for quantum cascade lasers. *Applied Physics Letters*, 104(3), 031907. doi:http://dx.doi.org/-10.1063/1.4863035.

[12] Brar, B., Kroemer, H., Ibbetson, J., & English, J. H. (1993). Photoluminescence from narrow InAs-AlSb quantum wells. *Applied Physics Letters*, 62(25), 3303-3305. doi:http://dx.doi.org/10.1063/1.109053.

[13] Junliang, X., Yu, Z., Yongping, L., Juan, W., Wei, X., Hongyue, H., . . . Zhichuan, N. (2014). Investigation of interfaces in AlSb/InAs/Ga0.71In0.29Sb quantum wells by photoluminescence. *Journal of Applied Physics*, 116(12), 123107. doi:http://dx.doi.org/-10.1063/1.4896553.

[14] Santos, P. V., Etchegoin, P., Cardona, M., Brar, B., & Kroemer, H. (1994). Optical anisotropy in InAs/AlSb superlattices. *Physical Review B*, 50(12), 8746-8754. doi:http://link.aps.org/doi/10.1103/PhysRevB.50.8746.

[15] Tuttle, G., Kroemer, H., & English, J. H. (1990). Effects of interface layer sequencing on the transport properties of InAs/AlSb quantum wells: Evidence for antisite donors at the InAs/AlSb interface. *Journal of Applied Physics*, 67(6), 3032-3037. doi:http://dx.doi.org/-10.1063/1.345426.

[16] Zhang, Y., Zhang, Y.-W., Wang, C.-Y., Guan, M., Cui, L.-J., Li, Y.-Y., . . . Zeng, Y.-P. (2013). High sensitivity Hall devices with AlSb/InAs quantum well structures. *Chinese*

Physics B, 22(5), 057106. doi:http://stacks.iop.org/1674-1056/22/i=5/a=057106.

[17] Sela, I., Bolognesi, C. R., Samoska, L. A., & Kroemer, H. (1992). Study of interface composition and quality in AlSb/InAs/AlSb quantum wells by Raman scattering from interface modes. *Applied Physics Letters*, 60(26), 3283-3285. doi:http://dx.doi.org/-10.1063/1.106720.

[18] Xu, D., Litvinchuk, A. P., Wang, X., Delaney, A., Le, H., & Pei, S. S. (2003). Structure stability of short-period InAs/AlSb superlattices. *Journal of Crystal Growth*, 251(1–4), 547-550. doi:http://dx.doi.org/10.1016/S0022-0248(02)02395-3.

[19] Barvosa-Carter, W., Twigg, M. E., Yang, M. J., & Whitman, L. J. (2001). Microscopic characterization of InAs/In0.28GaSb0.72/InAs/AlSb laser structure interfaces. *Physical Review B*, 63(24), 245311. doi:http://link.aps.org/doi/10.1103/PhysRevB.63.245311.

[20] Sato, A., Ohtani, K., Terauchi, R., Ohno, Y., Matsukura, F., & Ohno, H. (1999). X-ray diffraction study of InAs/AlSb interface bonds grown by molecular beam epitaxy. *Journal of Crystal Growth*, 201–202, 861-863. doi:http://dx.doi.org/10.1016/S0022-0248(98)01475-4.

[21] Chalmers, S. A., Kroemer, H., & Gossard, A. C. (1991). The growth of (Al,Ga)Sb tilted superlattices and their heteroepitaxy with InAs to form corrugated-barrier quantum wells. *Journal of Crystal Growth*, 111(1–4), 647-650. doi:http://dx.doi.org/10.1016/0022-0248(91)91057-H.

[22] Papa, N. Illustration of an interband optical transition in a type I finite quantum well syst em. Retrieved from https://commons.wikimedia.org/wiki/File:Interband_optical_transitio n.svg.

[23] Alexander, V. Intersubband optical transitions within a quantum cascade structure. Retrieved from https://commons.wikimedia.org/wiki/File:Cascade_transitions.svg.

[24] Faist, J. (2013). Quantum cascade lasers. *Oxford University Press*.

[25] Yang, R. Q. (1995). Infrared laser based on intersubband transitions in quantum wells. *Superlattices and Microstructures*, 17(1), 77-83. doi:10.1006/spmi.1995.1017.

[26] Canedy, C. L., Bewley, W. W., Lindle, J. R., Nolde, J. A., Larrabee, D. C., Kim, C. S., . . . Meyer, J. R. (2008). Interband Cascade Lasers with Wavelengths Spanning 2.9 μm to 5.2 μm. *Journal of Electronic Materials*, 37(12), 1780-1785. doi:10.1007/s11664-008-0444-1.

[27] Beere, H. E., Fowler, J. C., Alton, J., Linfield, E. H., Ritchie, D. A., Kohler, R., . . . Barbieri, S. (2005). MBE growth of terahertz quantum cascade lasers. *Journal of Crystal Growth*, 278(1-4), 756.

[28] Mukhopadhyay, P., Chowdhury, S., Wowchak, A., Dabiran, A., Chow, P., & Biswas, D. (2013). Dependence of structural and electrical properties of AlGaN/GaN HEMT on Si(111) on buffer growth conditions by MBE. *Journal of Vacuum Science & Technology B*, 31(3), 03C132. doi:http://dx.doi.org/10.1116/1.4803836.

[29] People, R., & Bean, J. C. (1985). Calculation of critical layer thickness versus lattice mismatch for GexSi1−x/Si strained-layer heterostructures. *Applied Physics Letters*, 47(3), 322-324. doi:http://dx.doi.org/10.1063/1.96206.

[30] Wasilewski, Z. R., Dion, M. M., Lockwood, D. J., Poole, P., Streater, R. W., & SpringThorpe, A. J. (1997). Composition of AlGaAs. *Journal of Applied Physics*, 81(4), 1683-1694. doi:http://dx.doi.org/10.1063/1.364012.

[31] Wasilewski, Z. R. (2016). Molecular Beam Epitaxy for quantum nano structures and devices.

[32] Friedrich, W., Knipping, P., Laue, M. V., & bei Röntgenstrahlen, I. E. (1912). Sitzungsberichte der Königlich Bayerischen Akademie der Wissenschaften. *Mathematische-Physische Klasse*, 42, 303-322.

[33] Amarasinghe, P., Qadri, S., & Wijewarnasuriya, P. (2015). High Resolution X-ray Diffraction Studies of MBE-Grown HgCdTe Layers on Bulk-Grown CdZnTe Substrate. *Journal of Electronic Materials*, 44(8), 2762-2767. doi:10.1007/s11664-015-3695-7.

[34] Liu, M., Ruan, H. H., Zhang, L. C., & Moridi, A. (2015). Temperature-dependent residual stresses in a hetero-epitaxial thin film system. *Thin Solid Films*, 584, 186-191.

doi:http://dx.doi.org/10.1016/j.tsf.2015.01.072.

[35] Jenkins, T. E. (1995). Semiconductor science: growth and characterization techniques. *Prentice-Hall*, Inc.

[36] GEN 10 MBE system Manual. *Veeco*, Inc.

[37] Vegar, O. (2011). Molecular Beam Epitaxy growth chamber. Retrieved from https://commons.wikimedia.org/wiki/File:MBE.png.

[38] Maissel, L. I., & Glang, R. (1995). Handbook of thin film technology.

[39] Dushman, S., Lafferty, J. M., & Brown, S. C. (1962). Scientific foundations of vacuum technique. *American Journal of Physics*, 30(8), 612-612.

[40] Loeb, L. B. (2004). The kinetic theory of gases. *Courier Corporation*.

[41] Wasilewski, Z. R., Aers, G. C., SpringThorpe, A. J., & Miner, C. J. (1991). Studies and modeling of growth uniformity in molecular beam epitaxy. *Journal of Vacuum Science & Technology B (Microelectronics Processing and Phenomena)*, 9(1), 120-131.

[42] Kumar, M., Rajpalke, M. K., Roul, B., Bhat, T. N., Kalghatgi, A. T., & Krupanidhi, S. B. (2012). Determination of MBE grown wurtzite GaN/Ge3N4/Ge heterojunctions band offset by X-ray photoelectron spectroscopy. *Physica Status Solidi (b)*, 249(1), 58-61.

[43] Zeindl, H. P., Nilsson, S., Klatt, J., Kruger, D., & Kurps, R. (2012). Influence of surfactants on molecular beam epitaxial grown SiGe single quantum wells studied by photoluminescence and secondary ion mass spectroscopy investigations. Selected Topics in *Group IV and II-VI Semiconductors*, 157, 31-35.

[44] Atenrok. (2013). Reflection high-energy electron diffraction. Retrieved from https://commons.wiki-media.org/wi-ki/File:Interband_optical_transition.svg.

[45] Tsang, W. T. (1984). Chemical beam epitaxy of InP and GaAs. *Applied Physics Letters*, 45(11), 1234-1236.

[46] Hass, G., Francombe, M. H., & Hoffman, R. W. (Eds.). (2013). Physics of thin films: advances in research and development. *Elsevier*.

[47] Kaganer, V. M., Köhler, R., Schmidbauer, M., Opitz, R., & Jenichen, B. (1997). X-ray diffraction peaks due to misfit dislocations in heteroepitaxial structures. *Physical Review B*, 55(3), 1793-1810.

[48] Hopkins, P. F., Rimberg, A. J., Westervelt, R. M., Tuttle, G., & Kroemer, H. (1991). Quantum Hall effect in InAs/AlSb quantum wells. *Applied Physics Letters*, 58(13), 1428-1430. doi:http://dx.doi.org/10.1063/1.105188.

[49] Johnson, S., Kuo, C.-H., Boonzaayer, M., Braun, W., Koelle, U., Zhang, Y.-H., & Roth, J. (1998). In situ temperature control of molecular beam epitaxy growth using band-edge thermometry. *Journal of Vacuum Science & Technology B (Microelectronics and Nanometer Structures)*, 16, 1502-1506.